THE ROLE OF FEEDBACK IN ASTROPHYSICS

THE ROLE OF FEEDBACK IN ASTROPHYSICS

By

MATTHEW LOW, B.SC.

A Thesis

Submitted to the School of Graduate Studies

in Partial Fulfilment of the Requirements

for the Degree

Master of Science

McMaster University

MASTER OF SCIENCE (2008) McMaster University

(Department of Physics and Astronomy) Hamilton, Ontario

TITLE: THE ROLE OF FEEDBACK IN ASTROPHYSICS

AUTHOR: Matthew Low, B.Sc.

SUPERVISOR: Dr. H. M. P. Couchman & Dr. J. W. Wadsley

NUMBER OF PAGES: xi, 81

Abstract

In very high resolution galaxy simulations, the supercomputers of today offer the possibility of enough resolution to capture the bubble of a supernova, though not the originating star itself. Modeling the energy released as originating from a single SPH particle initially arranged amongst a grid of particles requires the introduction of an artificial thermal conductivity term that allows the SPH method to resolve the thermal energy discontinuity inherently present in such a scenario. Such an artificial thermal conductivity is implemented in the SPH code GASOLINE. Resolution tests show that the method is insensitive to resolution changes when determining the radius of the Sedov-Taylor blast wave, and that the numerical solution agrees with the analytic prediction $R = \beta E^{1/5} \rho_0^{-1/5} t^{2/5}$. The peak density at the shock is lower than the actual value of four times the ambient density, though it is found to scale with resolution. The density of the interior of the shock, near the center of the supernova remnant is found to be elevated compared to the value expected from the Sedov-Taylor solution, but this too is resolution dependent, and with increased resolution the central density converges towards the expected value of zero. The fluid quantities pressure and velocity are also found to be in good agreement with the profiles predicted by the analytic solution.

Acknowledgements

The financial support, advice, and teaching provided by my advisers, Hugh Couchman and James Wadsley, has for the last two years allowed me to work in astrophysics. Without their generosity I would not have had the opportunity to do the work that is the topic of this thesis.

This work was made possible by the facilities and staff of the Shared Hierarchical Academic Research Computing Network (SHARCNET:www.sharcnet.ca).

Table of Contents

List of Figures

List of Tables

Chapter 1

Introduction

1.1 Energy injection in astrophysical processes

A main aim of many cosmological simulations, as well as a great deal of analytic and observational work, is to understand in detail how the structure visible today evolved from the initial density fluctuations, whose spectrum has become known thanks to the observations of the cosmic microwave background radiation. While dark matter shapes the gravitational wells in which visible matter evolves, it only weakly interacts with other matter through gravitational attraction; the evolution of visible structure is, in comparison, complicated greatly by feedback mechanisms, which serve to regulate the collapse of baryonic matter on all scales. In clusters of galaxies, the cooling intracluster medium can be radiatively heated to prevent its cooling onto galaxies by the output of active galactic nuclei (AGN; McCarthy et al. 2008). On the galactic scale, the winds emitted from an AGN can terminate the accretion onto the center black hole and expel the interstellar gas from the center of the galaxy

(Springel et al., 2005). The winds from massive stars can similarly regulate the star formation process in their star forming region, and in death can blow out as a supernova, the effects of which serve to both reduce the ability of the surrounding region to form stars through the reduction in available gas, and also to enhance the chance of stars being formed through the triggering of core collapse via the shocking of gas.

1.2 Active galactic nuclei

Active galactic nuclei inject large amounts of energy, in various forms, into their surroundings. The most obvious form of this output from Seyfert nuclei and quasars, which are highly luminous AGNs, is radiation. This type of feedback alters the environment of the AGN through both radiative pressure and radiative heating. In addition to this radiative output, AGN also present jets and winds, which are thought to be as important as feedback mechanisms as the radiative output of most accreting black holes (Begelman, 2003). The energy released by these objects is capable of regulating the dynamics of the intracluster medium.

The force exerted on gas due to radiation pressure is mediated through several processes. Electron scattering, scattering and absorption on dust, and photoionization all contribute to the pressure exerted by the radiation output from an AGN. The effects on dynamics of the gas in the host galaxy depends on the amount of radiation flux from the AGN compared to the Eddington limit of the black hole which powers it. For a flux that isn't much greater than the Eddington limit, the corresponding pressure can have only a small effect

on the hydrodynamics of the surrounding gas. Even for this case, however, the radiation pressure can exert considerable influence on the dust in the galaxy, whose cross section and thus the force it feels from the radiation is higher by five orders of magnitude (Dopita et al., 2002).

In addition to the pressure forces associated with the radiation output from AGN, the gas exposed to the radiation field is also subjected to a source of heating. The resultant hot gas has an equilibrium temperature set by the condition that the Compton cooling matches the inverse Compton heating, which for gases with typical AGN spectra can be on the order of 10^7 Kelvin (Begelman, 2003). Studying the interstellar medium of the galaxy as a whole, Begelman (1985) found that the X-ray heating resulting from AGN radiation output resulted in the elimination of cool ISM phases near the the central black hole, and the destruction of small clouds, leaving only giant molecular clouds in the interior regions of the galaxy. For some AGN, such as radio galaxies, the majority of the power of released is in the form of winds and jets (Rees et al., 1982). However, all accreting black holes may produce powerful outflows, such that the kinetic energy output of AGN is significant source of feedback (Begelman, 2003).

Since the timescale for the radiative cooling of gas in cluster cores is shorter than the Hubble time, an intracluster medium without any source of heating must tend towards the center of the cluster so that the ICM is in hydrostatic equilibrium (Begelman, 2003). However, the observations made with *Chandra* and $XMM - Newton$ show that the gas isn't free of heating. One attractive source of heating are AGNs, as radio galaxies are commonly found in the cen-

ters of clusters (Burns, 1990). These radio galaxies initially form supersonic stellar wind bubbles (Begelman & Cioffi, 1989), whose evolution can be described by the analytic Sedov-Taylor blast wave solution (described in §(2.2)). This solution is common to all feedback mechanisms which are characterized by the injection of a large amount of energy is a region small compared to the region over which the resulting effects are felt.

1.3 Supernovae and stellar winds

On a smaller scale, supernova and stellar winds introduce feedback into the evolution of the interstellar medium within galaxies. Although substantially different on small timescales, the result of both processes is to create a bubble in the ISM, whose evolution is given by the same Sedov-Taylor solution as for the evolution of the kinetic effects of AGN on their host galaxy. Several observations motivate the inclusion of feedback at this level, such as that 90% of stellar systems fail to evolve into open clusters (Lada & Lada, 2003). If the star forming region is initially gravitiationally bound, this implies that there is a process by which the gas in the star cluster is removed before futher star formation can be completed. This would also explain why the star formation in molecular clouds isn't very efficient (Fukui & Mizuno, 1991).

A few of the more recent developments in the study of galaxy formation, with highlights from work that demonstrates the key role supernova explosions play in galaxy development, span scales ranging from the determination of the properties of a multiphase interstellar medium (e.g. Wada & Norman (2001)) to the evolution of dwarf galaxies as a whole (Mac Low & Ferrara (1999) show

that supernova feedback can remove some or all of the gas in dwarf galaxies). Feedback has also been shown to interact dynamically with the dark matter in early galaxies to flatten central density cusps, which are not observed in nearby galaxies (Mashchenko et al., 2006).

1.4 Assessing the quality of feedback

One the many struggles of numerical methods is always against the available computing power. When Hernquist & Katz (1989) first started their galaxy simulations, they had a particle count in the thousands. The change in the number of particles one can feasibly use in a simulation is of course a rapidly moving barrier thanks to Moore's Law, but the number currently stands around the order of $10,000^3$ particles for a pure N-body simulation. For simulations with physical processes that have short dynamical timescales, that number can drop considerably; in the work done by Mashchenko et al. (2006), a simulation of 10^7 particles could take 600,000 CPU hours, with a stellar mass resolution of $100M_\odot$ and a gas mass resolution of $300M_\odot$.

The technological barrier that limits the practical resolutions possible in simulations motivates two behaviors in numerical methods - heuristics and investigations into minimal resolution requirements. Here, heuristic methods are defined as methods which replicate the effects of unresolvable physical processes on those that are resolved – i.e. heuristic methods are used to bring the effects of a sub-grid process up to a level where they can be resolved by the numerical method. Of course, when implementing a heuristic method for a large scale simulation, it can also be useful to run smaller scale simulations

to test if the heuristic method equates to the result of more basic physics. For the foreseeable future, the range of physical phenomenon that can be explicitly modeled within a global galaxy model will be a limited subset of all the physics that could be important to the evolution of the system, and it is knowing this that makes the ability to simulate physical processes with as little resolution as possible so valuable. Hence the ability to look at a situation where a large amount of energy is being released into a small volume, and watch as a numerical method evolved that most unresolved initial configuration into a physical solution is a rather desirable one.

In coming up with a scheme to bring these sub-grid processes up to a level where they can be resolved by the numerical method, there are additional numerical constraints that must be met in addition to the physical goals. The numerical goals not only include the necessity of being correct, but also a need to have an independence from resolution, or, failing that, at least the ability to converge to a single answer with increasing resolution. The sub-grid model should also be analogous to the physical process, so that where one might be used, if it were possible to have the resolution required, the other can replace it without changing the result.

The specific feedback mechanism that is the focus of this thesis is that of supernova explosions, but the general case of feedback arising from sub-grid processes all involve the release of a large amount of energy in a single smoothed particle hydrodynamics (SPH) particle. The solution to the problem of a detonation in which the energy is released in a negligibly small volume in a uniform density medium is known analytically: the Sedov-Taylor blast

wave model (Sedov, 1946). Against this solution the results of injecting a single SPH particle with a large amount of energy can be compared, though the solution is not what is expected from a supernova explosion in the galactic plane: there, the background density has an exponential profile. For this case too, however, there is an analytic solution (Kompaneets, 1960), allowing for a more realistic test of the effects of the death of a star.

The features of the shockwave that we wish to accurately reproduce are those that drive further physical evolution of the blast wave and its surroundings through their interaction with other physical processes. In particular, the density profile of the solution couples with cooling processes, such that it is important to generate a solution that is accurate particularly in the shock front, where the cooling of the gas is most intense, and where this cooling and the interaction with the surrounding medium will lead to instabilities. Equally important to cooling processes is the temperature of the gas in the blast wave. Lastly, the radius of the solution determines the scale over which the effects of the supernova explosion are important, which we wish to obtain so that multiple supernova events interact with a realistic timescale and frequence. Additionally, the blast radius determines the amount of material that is caught up in the explosion.

Recent work by Rosswog & Price (2007) and Price (2008) suggests that to be able to simulate accurately the Sedov-Taylor blast wave solution, the standard SPH equations must be modified. This thesis tests a number of initial SPH particle conditions run with both standard SPH and with a version of SPH that includes the modification proprosed in Price (2008), with the

aim of determining what is required to obtain the profiles of the important flow variables identified as density, temperature, and radius for the adiabatic explosion of a point-like source.

1.5 Blast waves as test cases

Together with the original Sedov-Taylor problem, the Kompaneets solution provides an excellent analytic test with which to qualitatively and quantitatively test the numerical solutions produced by SPH. The nature of these shocks, meaning the point-like dimensions of the initial explosion, in addition to the strength of the produced shock wave, makes them a significant challenge to try to simulate. In SPH, fluid quantities are best defined when they can be interpolated from several particles, making the initial condition for the Sedov-Taylor blast wave one of the worst possible; the injection of energy into a single SPH particle conflicts not only with the method's interpolation approach to finding fluid properties, but also the differential form of the fluid equations used in the formulation of SPH. Section §(3.1) gives an overview of smoothed particle hydrodynamics, and §(3.2) details the approach used in this thesis for solving the Sedov-Taylor blast wave problem.

A less specialized form of this test can be constructed in which the initial energy deposition is smoothed so as to not be singular in the sense of numerical resolution, but such a test is not particularly difficult, and most current smoothed particle and grid codes recover the analytic solution with such an initial condition (Tasker et al., 2008). In this thesis, these tests are not used primarily for the strength of shock, but to measure the performance

of Gasoline (the code used throughout this work) when strong thermal energy discontinuities are present. Two versions of Gasoline are tested, one with an artificial thermal conductivity term (Price, 2008) and one without. As such it is the injection of all the initial energy of the blast into a single particle that is the interesting feature of these tests.

Considering all of the possible methods by which a Sedov-Taylor blast wave problem can be set up for a SPH code, the focus of this thesis is on the a most extreme case. Three less specialized variants of the initial conditions were tested with Gasoline, where the initial energy was smoothed over the nearest neighbors of the source particle, and where the initial particle distribution is a glass instead of a grid (with both smoothed and unsmoothed energy injection). In all cases where the initial condition does not consist of a set of gridded particles with one single particle dominating the total energy of the particle ensemble, standard SPH reproduces the Sedov-Taylor blast wave solution without difficulty.

1.6 Outline

The purpose of the simulations reported in this thesis is to understand the requirements for modeling energy injection on sub-grid scales, including both resolution and initial particle configurations.

They underlying theoretical work that describes the basic physics in this thesis is presented in chapter 2. This will cover the form of the hydrodynamic equations, §(2.1), and more specific behaviors of the fluids obeying Euler's equations of motion are detailed in the subsequent subsections of that chapter. The directly relevant parts of the theory of Euler's equations include the equations for changes in the fluid variables as the flow passes through a shock, described in §(2.1.1). Once the basics of shock waves have been established, a specific case of shocking flows is described, a flow which results in the Sedov-Taylor blast wave, §(2.2). This case is extended to scenarios in which the background density is fitted by an exponential, rather than being constant, and is discussed in §(2.3).

After the basic physics has been covered, chapter 3 goes into depth as to how the fundamentals of fluid mechanics are used to actually numerically compute the properties of a flow, using the numerical method of Smoothed Particle Hydrodynamics (SPH), for which a brief introduction is given in §(3.1). After this section comes an overview of the artificial thermal conductivity addition made to the standard SPH equations so as to allow the modeling of point-like explosions in SPH simulations, in §(3.2). Following the discussion on artificial thermal conductivity is a section detailing how the need for such modifications to the SPH equations is limited in terms of being able to simulate a

Sedov-Taylor blast wave given different choices for the initial conditions of the simulation, §(4.1). The last section in chapter 3 shows how SPH reacts to a Sod shock tube (a particular flow problem commonly used as a test of numerical codes, described in Sod (1978)) with particles of differing mass in the left and right gas states, §(4.2).

Once the ideas behind artificial thermal conductivity have been reviewed in chapter 3, they are put into practice in several Gasoline runs, the results of which are reported in chapter 4. The tests performed included resolution tests, §(4.5), parameter evaluation runs, §(4.4), runs with initial particle distributions with are not grids, §(4.6), and detonations in an exponential atmosphere, §(4.7).

Lastly, the thesis is summarized in the conclusion, chapter 5

Chapter 2

Basic Physics

2.1 Hydrodynamics

The flow of inviscid ideal fluids is governed by the Euler equations, which specialize the conservation laws of mass, momentum, and energy for the hydrodynamic context. These laws can be formulated, respectively, as:

$$\frac{\partial \rho}{\partial t} + (\rho u_\alpha)_{,\alpha} = 0, \tag{2.1}$$

$$\frac{\partial \rho u_\alpha}{\partial t} + (\rho u_\alpha u_\beta)_{,\beta} + p_{,\alpha} = \rho f^b_\alpha, \tag{2.2}$$

$$\frac{\partial \rho E}{\partial t} + \{u_\alpha(\rho E + p)\}_{,\alpha} = \rho u_\alpha f^b_\alpha + \rho q; \tag{2.3}$$

where ρ is the fluid density, t is time, $\mathbf{u}$ is the velocity field with components u_α, p is the pressure, $\mathbf{f^b}$ the body force with components f^b_α, q the heating rate per unit mass, and E is the total energy. Repeated indices are taken to be indices of summation.

For three dimensional problems ($\alpha = 1, 2, 3$), equations (2.1) through (2.3) detail five conservation laws in six unknowns – ρ, u_α, p, and E. In the energy equation (2.3), the total energy E is defined as

$$E = e + \frac{1}{2} u_\alpha u_\alpha, \tag{2.4}$$

with e the internal energy of the system. Pressure, density, and internal energy are not all independent, and for an ideal gas equation of state with γ being the ratio of specific heats, they obey the relation

$$p = (\gamma - 1)\rho e. \tag{2.5}$$

The conservation laws (2.1) – (2.3) together with (2.5) fully describe the flow of ideal Eulerian fluids. Knowing the pressure and the density is enough to calculate the temperature of the fluid, using the ideal gas law

$$p = \frac{\rho R T}{\mu}, \tag{2.6}$$

where the temperature T is measured in Kelvin, R is the ideal gas constant $R = 8.3145 \times 10^7\ cm^2\ s^{-2}\ K^{-1}$ and μ the mean molecular mass (taken to be 0.62 throughout the work reported in this thesis).

2.1.1 Shock waves

Astrophysical flows are remarkable for the strong shocks that often develop in the interstellar medium, causing the flow variables such as velocity, pressure, and density, amongst others, to change discontinuously. In general, the discontinuities in a flow can be categorized into two types, one of which is

universally unstable and will spread to form a turbulent region, and the other corresponds to shocked flows (Landau & Lifshitz, 1987). For the general case, the locus of all points where the values of the fluid quantities are discontinuous defines a surface whose normal gives the direction of the discontinuities. Appropriately, such a surface is called a surface of discontinuity, and in general it can move throughout the fluid, unconstrained by the motion of the flow. A result of this is that particles may cross a surface of discontinuity, meaning that there must be boundary conditions that are satisfied on the surface.

One of these conditions is that the mass flux across the shock must be continuous. Denoting the two sides of the surface of discontinuity with suffixes 1 and 2, and adopting the notation $[\rho v_x] \equiv \rho_1 v_{1x} - \rho_2 v_{2x}$, we must have

$$[\rho v_x] = 0. \tag{2.7}$$

where the speeds v_{1x} and v_{2x} are the components of the flow velocities that are parallel to the surface normal of the shock, and are measured relative to the speed of the shock.

Both the energy and momentum fluxes are already known from the Euler equations for the conservation of energy (2.3) and momentum (2.2): the energy flux is $\mathbf{v}(\rho E + p)$, where the velocity variable has changed to $\mathbf{v}$ from $\mathbf{u}$ in (2.3), and the momentum flux along a unit vector $\mathbf{n}$ is $pn_i + \rho v_i v_k n_k$. The normal vector of the surface of discontinuity is parallel to the x-axis, so in that direction the momentum flux yields

$$[p + \rho v_x^2] = 0, \tag{2.8}$$

and the y and z components of the momentum flux yield

$$[\rho v_x v_y] = 0, \tag{2.9}$$

$$[\rho v_x v_z] = 0. \tag{2.10}$$

Before giving the boundary condition for the energy flux, it is convenient to rearrange its form slightly:

$$\mathbf{v}(\rho E + p) = \rho \mathbf{v} \left(\frac{1}{2} v^2 + e + p/\rho \right).$$

Taking $e + p/\rho = w$, the requirement that the energy flux be continuous across the surface of discontinuity means that

$$\left[\rho v_x \left(\frac{1}{2} v^2 + w \right) \right] = 0. \tag{2.11}$$

The two types of surface of discontinuity are delineated by the mass flux through the surface. If the mass flux is zero, Landau & Lifshitz (1987) show that v_y and v_z are discontinuous across the surface, and go on to show that such a tangential discontinuity is unstable for all velocities. In the case where the mass flux is not zero, the continuity conditions are equivalent to

$$[\rho v_x] = 0, \tag{2.12}$$

$$[p + \rho v_x^2] = 0, \tag{2.13}$$

$$\left[\frac{1}{2} v_x^2 + w \right] = 0. \tag{2.14}$$

Given the tendency for astrophysical flows to form strong shocks, it would be nice to specialize the boundary conditions such that we know the behavior

of the fluid quantities on either side of a high Mach number shock (where a high Mach number is defined by equations (2.26) and (2.27)). Dropping the bracket notation, and letting v_x become simply v as it is now the only component of the velocity that changes across the shock, (2.12) – (2.14) become

$$\rho_1 v_1 = \rho_2 v_2, \tag{2.15}$$

$$p_1 + \rho_1 v_1^2 = p_2 + \rho_2 v_2^2, \tag{2.16}$$

$$w_1 + \frac{1}{2} v_1^2 = w_2 + \frac{1}{2} v_2^2. \tag{2.17}$$

From these the following are easily obtained:

$$\rho_1 v_1^2 - \rho_2 v_2^2 = p_2 - p_1, \tag{2.18}$$

$$w_1 - w_2 + \frac{1}{2}(v_1^2 - v_2^2) = 0. \tag{2.19}$$

An equation that will be useful is

$$\left(\frac{1}{\rho_1} + \frac{1}{\rho_2}\right)(\rho_1 v_1^2 + \rho_2 v_2^2) = v_1^2 - \frac{\rho_2}{\rho_1} v_2^2 + \frac{\rho_1}{\rho_2} v_1^2 + v_2^2, \tag{2.20}$$

which can be simplified using (2.15) to give $\frac{\rho_1}{\rho_2} v_1^2 = v_2 v_1$ and similarly $\frac{\rho_2}{\rho_1} v_2^2 = v_1 v_2$. Substituting these into (2.20),

$$\left(\frac{1}{\rho_1} + \frac{1}{\rho_2}\right)(\rho_1 v_1^2 + \rho_2 v_2^2) = v_1^2 - v_2^2, \tag{2.21}$$

so that

$$v_1^2 - v_2^2 = \left(\frac{1}{\rho_1} + \frac{1}{\rho_2}\right)(p_2 - p_1) \tag{2.22}$$

by way of (2.18). Defining $V_1 = 1/\rho_1$ and $V_2 = 1/\rho_2$,

$$w_1 - w_2 + \frac{1}{2}(V_1 + V_2)(p_2 - p_1) = 0 \tag{2.23}$$

follows from the substituting of (2.22) into (2.19).

For the flows which have a constant γ and are adiabatic, $w = \gamma pV/(\gamma - 1)$ (Landau & Lifshitz, 1987). Substitution into (2.23) gives

$$\frac{V_2}{V_1} = \frac{(\gamma + 1)p_1 + (\gamma - 1)p_2}{(\gamma - 1)p_1 + (\gamma + 1)p_2}, \tag{2.24}$$

which can be used to find the ratio of the temperatures across the shock for an ideal gas where $T_2/T_1 = p_2V_2/p_1V_1$:

$$\frac{T_2}{T_1} = \frac{p_2}{p_1}\frac{(\gamma + 1)p_1 + (\gamma - 1)p_2}{(\gamma - 1)p_1 + (\gamma + 1)p_2}. \tag{2.25}$$

These equations yield the limiting results for extreme shock waves, which are characterized by the condition that $(\gamma-1)p_2 \gg (\gamma+1)p_1$. When this condition is satisfied,

$$V_2/V_1 = \rho_1/\rho_2 = (\gamma - 1)/(\gamma + 1), \tag{2.26}$$

$$T_2/T_2 = (\gamma - 1)p_2/(\gamma + 1)p_1. \tag{2.27}$$

2.2 Sedov-Taylor blast wave

During a supernova explosion in a uniform density interstellar medium, the blast radius quickly becomes enormous compared the the dimensions of the dying star. In the regime where the wave is not too distant from the source, so that the shock strength is still large (though still distant enough so that the dimensions of the source are negligible), we can describe the supernova as a Sedov-Taylor blast wave. The solution is self-similar, derived in an analytic form independently by von Neumann (1941) and Sedov (1946). Earlier work

done by Taylor (1950) was completed in 1941, though not published until 1950, and provides a simple method of deriving the approximate dependence of the blast wave radius on time using dimensional analysis.

As a result of the assumption of a strong shock, the pressure discontinuity across the pre- and post-shock boundary is guaranteed to be large. To formalize the meaning of a 'strong shock' in this problem, take the ratio of the pressure p_2 behind the shock to the pressure p_1 in front of the shock to be such that

$$p_2/p_1 \gg (\gamma+1)/(\gamma-1). \tag{2.28}$$

As shown in 2.1.1, this means that the density ratio ρ_2/ρ_1 reaches its limiting value of $(\gamma+1)/(\gamma-1)$, and so $\rho_2 = 4\rho_1$ for a monatomic gas ($\gamma = 5/3$) or $\rho_2 = 6\rho_1$ for a diatomic gas ($\gamma = 7/5$).

2.2.1 Dimensional analysis

Since the problem is defined such that p_1 is always negligible compared to p_2, there are only two parameters that can influence the movement of the shock wave, those being the initial gas density ρ_1 and the energy released by the supernova, E. With these quantities and also considering the time t elapsed since the star went supernova, we can perform the dimensional analysis first done by Taylor (1950). The only combination of E, ρ_1 and t that has units of length is $E^{1/5}t^{2/5}\rho_1^{-1/5}$, and so we must have for the radius of the shock wave

$$R = \beta\left(\frac{E}{\rho_1}\right)^{1/5} t^{2/5}. \tag{2.29}$$

Due to the spherical symmetry of the problem, the motion is one-dimensional along the radial coordinate.

2.2.2 Analytic solution

In (2.29), the constant of proportionality, β was left undetermined, awaiting a full solution to the problem. Both Sedov (1946) and von Neumann (1941) independently arrived at an analytic solution to the equations of motion for a fluid for which the condition (2.28) is well satisfied. Following their solution, as presented in Landau & Lifshitz (1987), β is given by

$$\beta^5 \frac{16\pi}{25} \int_0^1 G \left[\frac{1}{2} V^2 + \frac{Z}{\gamma(\gamma - 1)} \right] \xi^4 \, \mathrm{d}\xi = 1. \tag{2.30}$$

The integration is over the variable ξ, which is the scaled radial coordinate,

$$\xi = r/R = (r/\beta)(\rho_1 / E t^2)^{1/5}, \tag{2.31}$$

and the variables Z, V, and G are defined by

$$Z = \frac{\gamma(\gamma - 1)(1 - v)V^2}{2(\gamma V - 1)},$$

$$\xi^5 = [\frac{1}{2}(\gamma - 1)V]^{-2} \left\{ \frac{\gamma + 1}{7 - \gamma} [5 - (3\gamma - 1)V] \right\}^{\nu_1} \left[\frac{\gamma + 1}{\gamma - 1} (\gamma V - 1) \right]^{\nu_2},$$

$$G = \frac{\gamma + 1}{\gamma - 1} \left[\frac{\gamma + 1}{\gamma - 1} (\gamma V - 1) \right]^{\nu_3} \left\{ \frac{\gamma + 1}{7 - \gamma} [5 - (3\gamma - 1)V] \right\}^{\nu_4} \left[\frac{\gamma + 1}{\gamma - 1} (1 - V) \right]^{\nu_5},$$

$$\nu_1 = -\frac{13\gamma^2 - 7\gamma + 12}{(3\gamma - 1)(2\gamma + 1)},$$

$$\nu_2 = \frac{5(\gamma - 1)}{2\gamma + 1},$$

$$\nu_3 = \frac{3}{2\gamma + 1},$$

$$\nu_4 = -\frac{\nu_1}{2 - \gamma},$$

$$\nu_5 = -\frac{2}{2 - \gamma}. \tag{2.32}$$

Equations (2.32) and (2.30) show that β depends only on γ

In addition to determining the value of β for a given γ, V, G, and Z describe the behavior of the flow inside the shock radius R. The values of the fluid velocity, v, density ρ and sound speed c inside the shock front are given by

$$v = 2rV/5t, \tag{2.33}$$

$$\rho = \rho_1 G, \tag{2.34}$$

$$c^2 = 4r^2 Z/25t^2. \tag{2.35}$$

The pressure in the region behind the shock can be recovered from (2.35) as $c^2 = \gamma p/\rho$.

Figure 2.1 shows the values of v, ρ, and p inside the blast wave, where the values have been normalized to their immediate post-shock values and are plotted against ξ.

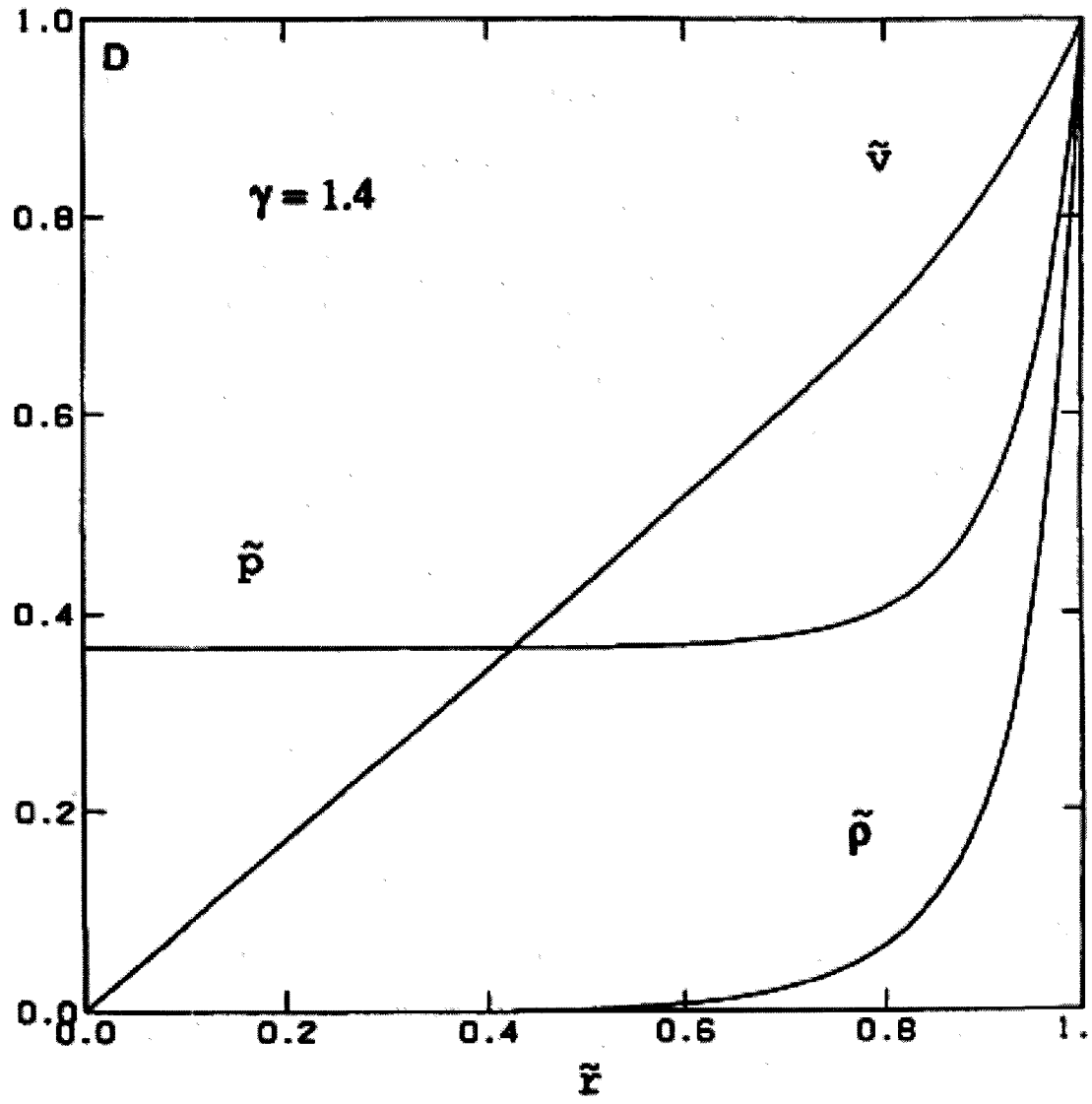

Figure 2.1: Normalized flow variables for $\gamma = 1.4$. The quantities in the figure, $\tilde{\rho}$, $\tilde{p}$ and $\tilde{v}$ are the normalized values of ρ, p and v given by (2.33)–(2.35), and $\tilde{r}$ corresponds to ξ. This figure is from Ryu & Vishniac (1987), in which it appears as Fig. 1.

2.3 Detonations in an exponential atmosphere

Despite the successes of the Sedov-Taylor solution, many interesting astrophysical problems occur in an ambient medium which is not uniform. Perhaps the most ubiquitous condition in which galaxy simulations are run is a disk structure, either assumed beforehand or evolved from more basic conditions. This structure leads to a hydrostatic solution with an atmospheric density given by an exponential of the form

$$\rho = \rho_0 e^{-z/h}, \tag{2.36}$$

with z being the coordinate along the gradient of the density and h the scale height of the atmosphere. The ability of an exponential atmosphere to model the H I gas in the Galaxy has been tested, and found to be lacking (Dickey & Lockman, 1990). Fortunately, of the three scale heights that characterize the three exponentials which form the basis of the density distribution put forth in (Dickey & Lockman, 1990), the smallest corresponds to an exponential atmosphere. In the regime where the gas distribution is roughly exponential, we can use the work of Kompaneets (1960) and later investigations from Maciejewski & Cox (1999), who derive how a point explosion propagates into an exponential atmosphere. A sketch of the problem including the relevant quantities is given in figure 2.2, which comes from Maciejewski & Cox (1999).

In order to arrive at the results of Kompaneets (1960), Maciejewski & Cox (1999) assume a density of the form given in (2.36), with ρ_0 being taken as the density at the initial explosion point. The point on the shock that expands into the most rarefied background gas is a distance z_L from the origin of the

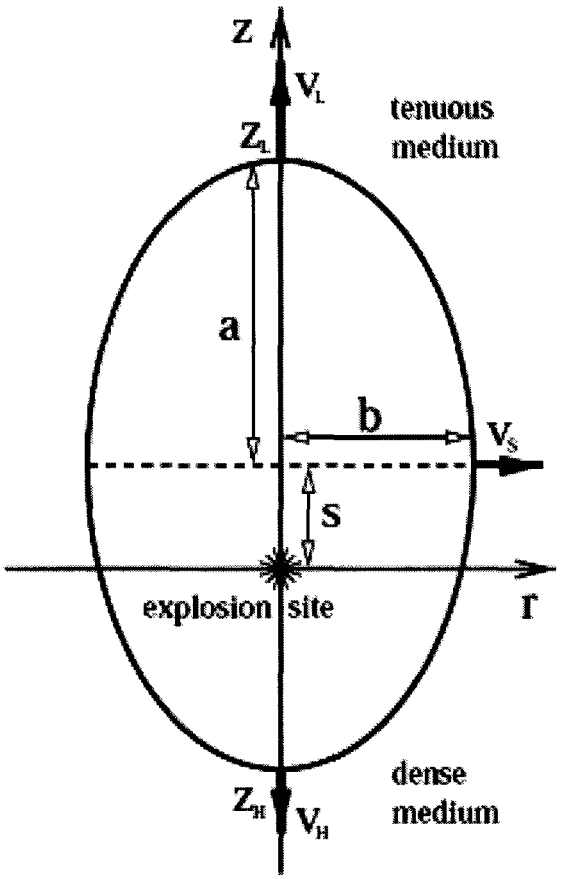

Figure 2.2: A sketch of the solution to the problem of a point explosion in an exponential atmosphere. From Maciejewski & Cox (1999).

blast, and complementing z_L is z_H, the distance to the point on the shock that is pushing into the most dense medium (figure 2.2 has a schematic of the situation with the quantities of interest labeled). The velocities of the shock at these points are v_L and v_H. The semi-major axis of the shock wave is then found through $2a = z_L - z_H$. The rest of the labeled quantities are b, the semi-minor axis, s the distance between the initial explosion point at the plane that cuts through the widest part of the shock (which shall be referred to as the equator of the shock), and v_s, the speed of the shock at its equator.

The pressure behind a strong shock $p-2$ in a $\gamma = \frac{5}{3}$ ideal gas is related to the the density of the medium into which the shock is propagating ρ_1 and the velocity of the shock v by the equation (Spitzer, 1978)

$$p_2 = \frac{3}{4}\rho_1 v^2. \tag{2.37}$$

If the various post shock pressures that result from the interplay between the exponential form of ρ_1 and variable shock velocity v are all the same (though not constant), then the resultant shock form is that given by Kompaneets (1960). In this case the shock speed varies along the shock so that

$$v = \sqrt{\frac{4p_2}{3\rho_1}}, \tag{2.38}$$

which we can write in terms of the unperturbed density at the source ρ_0 using (2.36)

$$v = \sqrt{\frac{4p_2}{3\rho_0}} e^{\frac{z}{2h}}. \tag{2.39}$$

From the velocity function the rates of change of the axes of the shock follow, with the expansion rate of the semi-major axis $\dot{a}$ being the average of the velocity of the endpoint's of the axis,

$$\dot{a} = \frac{1}{2}(v_H + v_L) = \frac{1}{2}\sqrt{\frac{4p_2}{3\rho_0}}\left(e^{\frac{z_H}{2h}} + e^{\frac{z_L}{2h}}\right). \tag{2.40}$$

The equatorial velocity gives the rate of change of the semi-minor axis $\dot{b}$

$$\dot{b} = v_s = \sqrt{\frac{4p_2}{3\rho_0}}e^{s/2h}, \tag{2.41}$$

and the change in the distance between the source and the equator again depends on the expansion along a, except that if both ends of the shock expand at the same rate, the s remains unchanged, so that instead of (2.40), the equation takes the form

$$\dot{s} = \frac{v_L - v_H}{2} = \frac{1}{2}\sqrt{\frac{4p_2}{3\rho_0}}\left(e^{\frac{z_H}{2h}} + e^{\frac{z_L}{2h}}\right). \tag{2.42}$$

The number of variables in the solution can be reduced by writing $z_H = s - a$ and $z_L = s + a$. With these substitutions, we can combine (2.40) and (2.41) give a solution for either a or b given the other,

$$\frac{\mathrm{d}b}{\mathrm{d}a} = \mathrm{sech}\frac{a}{2h}, \tag{2.43}$$

or, integrating,

$$\tan\frac{b}{2h} = \sinh\frac{a}{2h} \tag{2.44}$$

Similarly, (2.42) and (2.40) yield

$$e^{s/2h} = \cosh\frac{a}{2h}. \tag{2.45}$$

Chapter 3

Methods

3.1 Smoothed Particle Hydrodynamics

Several methods have been devised which focus on finding approximate solutions to the equations of fluid dynamics given in §(2.1), and various codes have been written to exploit the fairly well established techniques of finite difference and finite volume schemes applied towards the goal of capturing the behavior of complicated fluid dynamics. A relatively modern reference for such methods can be found in Wesseling (2001). Smoothed Particle Hydrodynamics (SPH) takes a markedly different approach to the same problem, employing an interpolation algorithm to replace the fluid with a discrete set of particles over which the flow quantities are distributed. This method of calculating the equations of motion for fluids was independently arrived at by Gingold & Monaghan (1977) and Lucy (1977), and for which Monaghan (1992) gives a thorough review.

3.1.1 Interpolation

In §(2.1), the rates of change of the fluid variables can be seen to require the spatial derivatives of various quantities, and so regardless of the method used to numerically solve the equations of motion, approximate values for these derivative will have to be found (Monaghan, 2005). The striking difference between SPH and finite difference methods is rooted in how the derivatives are evaluated. Finite difference methods approximate the derivatives at a finite number of points which are the vertices of a grid, an approach that the SPH algorithm completely ignores, instead transferring the derivative terms onto the kernel function. The kernel function is then used in an interpolation operation to generate gradients, with the interpolation points being the particles that sample the fluid properties.

3.1.1.1 Integral Interpolation

The interpolation that SPH approximates is defined by

$$A_I(\mathbf{r}) = \int A(\mathbf{r}')W(\mathbf{r}-\mathbf{r}', h)\,\mathrm{d}\mathbf{r}' \tag{3.1}$$

where A_I is the interpolated value of A at $\mathbf{r}$, A being a generic quantity of interest. W is the kernel function, which depends on the displacement between the interpolation point and the location of the infinitesimal volume element $\mathrm{d}\mathbf{r}'$, as well as a length scale h, which characterizes the response of W to a given displacement. In practice the kernel is taken to be radially symmetric, so that $W(\mathbf{r}-\mathbf{r}', h) = W(r, h)$ with r the distance between $\mathbf{r}$ and $\mathbf{r}'$. The code used for the work done in this thesis (Gasoline, c.f. Wadsley et al. 2004) implements

this symmetry through a kernel-averaging as proposed by Hernquist & Katz (1989):

$$W_{ij} = \frac{1}{2}w(|\mathbf{r}_i - \mathbf{r}_j|/h_i) + \frac{1}{2}w(|\mathbf{r}_i - \mathbf{r}_j|/h_j). \tag{3.2}$$

The integration is performed over all space, and the generic properties of W are that it tends to the delta function for $h \to 0$, and is normalized:

$$\int W(\mathbf{r} - \mathbf{r}', h)\, \mathrm{d}\mathbf{r}' = 1. \tag{3.3}$$

As such, the equation SPH seeks to approximate, (3.1), is itself an approximation of the identity

$$A(\mathbf{r}) = \int A(\mathbf{r}')\delta(\mathbf{r} - \mathbf{r}')\, \mathrm{d}\mathbf{r}'. \tag{3.4}$$

One of the more common kernels that can be found in SPH codes, and is the one used in Gasoline, is the cubic spline (Monaghan, 1992): with q defined as $q = |x|/h$, the cubic spline has the form (in three dimensions)

$$M_4(x) = \begin{cases} \frac{1}{4\pi h^3}(2-q)^3 - 4(1-q)^3, & \text{for } 0 \le q \le 1, \\ \frac{1}{4\pi h^3}(2-q)^3, & \text{for } 1 \le q \le 2, \\ 0, & \text{for } q \ge 2. \end{cases} \tag{3.5}$$

3.1.1.2 Summation Interpolation and the Discrete Equations of Motion

In order to discretize the SPH algorithm, the interpolation integrals for any quantity need to be modified so that they integrate over infinitesimal masses rather than volumes. Accordingly, let (3.1) be re-written as

$$A_I(\mathbf{r}) = \int \frac{A(\mathbf{r}')}{\rho(\mathbf{r}')} W(\mathbf{r} - \mathbf{r}', h)\rho(\mathbf{r}')\, \mathrm{d}\mathbf{r}' \tag{3.6}$$

for which the summation interpolant is obtained immediately by noting that $\rho(\mathbf{r}')\,\mathrm{d}\mathbf{r}'$ is simply a mass element:

$$A_s(\mathbf{r}) = \sum_b m_b \frac{A_b}{\rho_b} W(\mathbf{r} - \mathbf{r}_b, h) \tag{3.7}$$

One feature of SPH is that there is a lot freedom of choice when it comes to choosing the exact form of the equation of motion of the system, and it can be beneficial to examine the various vector identities that transform equations from one form to another and allow for the exploitation of symmetric (and hence explicitly conservative) energy and momentum equations. With these considerations, Gasoline evolves hydrodynamical quantities with the following equations (Monaghan, 1992).

Density is calculated from the sum

$$\rho_i = \sum_{j=1}^{n} m_j W_{ij}. \tag{3.8}$$

which follows directly from the interpolation sum given by (3.7). The momentum equation takes the form

$$\frac{\mathrm{d}\mathbf{v}_i}{\mathrm{d}t} = -\sum_{j=1}^{n} m_j \left(\frac{P_i}{\rho_i^2} + \frac{P_j}{\rho_j^2} + \Pi_{ij} \right) \nabla_i W_{ij}, \tag{3.9}$$

with the usual symbol notation, P_j is pressure, and $\mathbf{v}_i$ velocity. Π_{ij} is designed to mimic viscous forces, though for now the discussion of it is put off until section §(3.1.2).

The energy equation is expressed in a slightly dissimilar manner compared to (3.9), instead using a form found in Evrard (1988), which is both explicitly

energy conserving, and also independent of non-local pressures (which has the nice result that the energy can't be driven negative by large pressure gradients).

$$\frac{\mathrm{d}u_i}{\mathrm{d}t} = \frac{P_i}{\rho_i^2} \sum_{j=1}^{n} m_j \mathbf{v}_{ij} \cdot \nabla_i W_{ij}, \tag{3.10}$$

with u_i the internal energy of the i^{th} particle.

3.1.2 Artificial viscosity

Lucy (1977) first introduced an artificial viscosity into SPH to help with the stabilization of solutions, which remains one of the two most common uses for such a term. The other use is to allow the SPH equations to capture shocks, which is the main purpose of the Π_{ij} term in (3.9). In Gasoline, the artificial viscosity is formulated as:

$$\Pi_{ij} = \begin{cases} \frac{-\alpha \frac{1}{2}(c_i + c_j)\mu_{ij} + \beta \mu_{ij}^2}{\frac{1}{2}(\rho_i + \rho_j)} & \text{for } \mathbf{v}_{ij} \cdot \mathbf{r}_{ij} < 0, \\ 0 & \text{otherwise,} \end{cases} \tag{3.11}$$

with

$$\mu_{ij} = \frac{h(\mathbf{v}_{ij} \cdot \mathbf{r}_{ij})}{\mathbf{r}_{ij}^2 + 0.01(h_i + h_j)^2}, \tag{3.12}$$

and $\mathbf{r}_{ij} = \mathbf{r}_i - \mathbf{r}_j$; $\mathbf{v}_{ij} = \mathbf{v}_i - \mathbf{v}_j$; c_j is the sound speed. The term $0.01(h_i + h_j)^2$ serves to prevent singularities. A large number of simulations have shown that values of α and β of 1 and 2 respectively works for most problems.

The use of artificial viscosity to capture shocking phenomenon is particularly important to this work, as the proposed thermal conductivity acts in an analogous manner for discontinuities in thermal energy, whereas the viscosity term smooths discontinuities in the momentum distribution.

3.2 Artificial thermal conductivity

Artificial thermal conductivity has been advocated recently by (Rosswog & Price, 2007) and (Price, 2008) as a method to deal with numerical artifacts that become important when a flow has large discontinuity in thermal energy, or flows that are sensitive to small discontinuities. Price (2008) cites several fluid dynamics problems that have proven difficult to treat with SPH methods, including the the simulation of Kelvin-Helmholtz instabilities (a problem highlighted by Agertz et al. 2007), as well as multi-phase flows (Ritchie & Thomas 2001; Marri & White 2003), which have been more effectively simulated with the inclusion of an extra diffusion term into the SPH equations.

At the heart of the argument for the inclusion of artificial thermal conductivity made in (Price, 2008) is the idea that SPH can be derived from a Lagrangian variational principle. Immediately this implies that the action must disappear on the surface of the volume of interest, so that the surface integral terms in the variational procedure vanish. One example given in (Price, 2008) is that of the SPH continuity equation:

$$\frac{d}{dt}\sum_j mjW_{ij} = \sum_j m_j(\mathbf{v}_i - \mathbf{v}_j)\cdot\nabla W_{ij} - \int[\rho'\mathbf{v}'W]\cdot\mathrm{d}\mathbf{S}. \tag{3.13}$$

Usually the compact support of the kernel function means that the surface integral is identically zero, but in the case of a discontinuity, any SPH formulas which assume differentiability will suffer an ignorance of the discontinuity. This isn't a new problem with SPH though, and as mentioned above in §(3.1.2), the use of numerical diffusion to smear out discontinuities so as they may be resolved by a differential system has long been in practice with numerical

viscosity. Earlier work by Monaghan (1997) provides dissipative terms in the rates of change of momentum and energy

$$\left(\frac{d\mathbf{v}_i}{dt}\right)_{diss} = \sum_j m_j \frac{\alpha v_{sig}(\mathbf{v}_i - \mathbf{v}_j)\cdot \hat{\mathbf{r}_{ij}}}{\bar{\rho_{ij}}} \nabla_i W_{ij}, \tag{3.14}$$

$$\left(\frac{d\mathbf{e}_i}{dt}\right)_{diss} = \sum_j m_j \frac{(\mathbf{e}_i^* - \mathbf{e}_j^*)}{\bar{\rho_{ij}}} \hat{\mathbf{r}_{ij}} \cdot \nabla_i W_{ij}, \tag{3.15}$$

with the restriction the here the kernel must be symmetric (which is true for Gasoline). Also, e_i^* isn't exactly the internal energy, it is something that has the form of internal energy, but only includes quantities that have components along the radius vector between particles i and j, $e_i^* = \frac{1}{2}\alpha v_{sig}(\mathbf{v}_i \cdot \hat{\mathbf{r}_{ij}})^2 + \alpha_u v_{sig}^u u_i$. The choice of v_{sig} is made to eliminate the diffusion terms away from discontinuities where it is unwanted. From the thermal energy equation,

$$\frac{du}{dt} = \frac{de}{dt} - \mathbf{v}\cdot\frac{d\mathbf{v}}{dt}, \tag{3.16}$$

and the dissipation equations, Price derives a dissipative term for thermal energy which will be the focus of the work in this thesis.

$$\left(\frac{du}{dt}\right)_{diss} = -\sum_j \frac{m_j}{\bar{\rho_{ij}}} \left\{\frac{1}{2}\alpha v_{sig}(\mathbf{v}_{ij}\cdot\hat{\mathbf{r}_{ij}})^2 + \alpha_u v_{sig}^u (u_i - u_j)\right\} \hat{\mathbf{r}_{ij}} \cdot \nabla_i W_{ij}, \tag{3.17}$$

where the term expressed as a difference of energies is the form of artificial thermal conductivity that used throughout most of the paper. α_u is a tunable parameter to adjust the strength of the diffusion term. In §4, it is found that a value of 1 works well.

3.2.1 Signal velocities

A major disadvantage to all dissipative terms is that they work to smooth out all gradients, whether they represent a discontinuous phenomenon or not. With artificial viscosity, this problem is alleviated by the fact that shock gradients are continually steepened as the wave propagates. Unfortunately, a gradient in the thermal energy has no such property, so that they are permanently reduced if diffused. So as to avoid excess diffusion, the signal velocity term in (3.17) is constructed so that it is zero away from discontinuities. Since pressure is continuous across a contact discontinuity, a signal velocity of the form (Price, 2008)

$$v_{sig}^{u} = \sqrt{\frac{|P_i - P_j|}{\bar{\rho}_{ij}}}, \tag{3.18}$$

will prevent spurious diffusion in cases where pressure gradients are not being balanced be external forces, for example gravity. In cases where they are, alternate forms of the v_{sig}^{u} may be substituted.

It is interesting to look back at the start of this section, where it was stated that the SPH formalism is heavily abstracted away from the idea of discretizing space in order to directly evaluate derivatives. While much has been said about how SPH ignores discontinuities as a method derived from a Lagrangian, SPH does not fail when the a form of an interpolation equation is not consistent with one derived from a Lagrangian. In this light it is not obvious that introducing yet more artificial dissipation into the numerical workings of simulation codes is the only solution there is to this problem. In the conclusion of Price (2008), several alternative approaches are mentioned which are interesting in their own right, though as this thesis doesn't consider them

they will only be mentioned briefly. The first of these other trains of thought considers that artificial conductivity is a solution to an already known problem in SPH, that of an effective surface tension at phase boundaries and discontinuities, and that a resolution to this excess tension could resolve many of the same problems that artificial thermal conductivity addresses (see Hu & Adams (2006) for more detailed information on the tension forces in SPH).

Alternatively, one could go for the direct approach and calculate the surface integrals (along the lines of Katz (2001)), or else try to merge SPH with a Godunov scheme (a numerical approach to solving the Riemann problem across a cell boundary so as to evolve the fluid state on both sides of the boundary) and solve the Riemann problem for pairs of particles (Inutsuka, 2002).

Chapter 4

Results

The aims of these point-explosion simulations are two-fold: the faithful reproduction of a Sedov-Taylor blast wave, the analytic form of which is given in §(2.2) constitutes the physical goal. The other criterion required of reliable simulations is an independence of resolution, or at least a convergence to a single solution with increasing resolution. The ability, or lack thereof, of standard SPH to form a physical solution to the problem of the point injection of energy into a single SPH particle in an array of gridded particles is a primary motivation for the development of a thermal conductivity term. To test this, two sets of simulations were run, the first of which uses a set of particles which are initially gridded. A second test of Gasoline using standard SPH shows that the initial particle distribution has a marked effect on the numerical solution. After testing the results of Gasoline implementing the standard SPH equations using an initially gridded set of particles, the same initial condition is tested with Gasoline with a thermal conductivity term added to the SPH formalisms. These tests are separated into two sets; the first determines the value of α_u, the thermal conductivity parameter that scales the magnitude of

the artificial thermal conductivity term, given by equation (3.17). The second tests the effects of resolution on the result of the simulation.

Lastly, a point explosion is set off in an exponential atmosphere using an initial condition in which the particles are gridded. The initial conditions are evolved with the artificial thermal conductivity term. This is the only test which requires a system of units, and the test is designed to be comparable to the work of another group working with a grid code, ZEUS-MP. The results of Gasoline with thermal conductivity are compared to both the ZEUS-MP results and the analytic Kompaneets solution.

4.1 Initial conditions

Four types of initial conditions were tested for the Sedov-Taylor blast wave problem. Of these four sets of initial conditions, only one proved difficult to simulate; for the case where the initial distribution of particles is on a grid, with the blast energy originally concentrated in a single particle on this grid, Gasoline implementing the standard SPH equations could not reproduce the correct dependence of the shock radius with time nor energy, $R \propto E^{1/5}$ and $R \propto t^{2/5}$.

The other three types of initial condition varied the particle arrangement and how the initial energy was deposited among the particles of the simulation. These variations were tested with Gasoline using the initial conditions:

- gridded particles, blast energy smoothed over the nearest neighbors of the source particle ;

- glass particle distribution, blast energy smoothed over the nearest neighbors of the source particle ;

- glass particle distribution, blast energy concentrated in a single source particle.

For theses simulations, the radial profiles of the gas density, pressure, velocity, and internal energy agree with the analytic solutions given in §(2.2). Tasker et al. (2008) shows that several SPH codes using an initial condition with particles relaxed into a glass and the blast energy added to 32 central particles perform similarly to Gasoline, and reinforces the fact that, with a suitable choice of initial conditions, this problem isn't a difficult one for SPH methods.

In addition to testing Gasoline, another SPH code, Gadget2, which evolves an entropy equation instead of the thermal energy (Springel & Hernquist, 2002), was run with the gridded particle initial conditions for the Sedov-Taylor blast wave test, with the energy deposited into a single SPH particle. The same problems were encountered with that code as were found with gasoline: the blast wave had severe radial asymmetries. Attempts to increase the artificial viscosity to prevent the particles from penetrating the shock wave were unsuccessful for both codes.

The type of initial condition that is the focus of this work does not smooth out the initial energy deposition, nor does it attempt to relax the SPH particles into a glass before the simulation begins. It is for this problem, where the particles are initially gridded and where a single particle is injected with the blast energy, that a thermal conductivity term must be implemented.

4.2 Variable mass particles

One method of reducing the number of particles required in a simulation is to selectively increase the mass of particles in regions of the simulation where the resolution required is less than in more dynamic regions. However, if these sets of particles mix, the result is to have low resolution particles interacting with high resolution particles. As a simple test to gauge the behavior of SPH when particles of differing mass resolution are mixed, a variable mass Sod shock tube problem (Sod, 1978) was set up. The Sod shock tube consists of a box with a left and a right state. The states are defined by their flow variables, which are (with l subscripts denoting left state variable, and r subscripts the right state variables)

$$u_l = 0, \qquad u_r = 0, \tag{4.1}$$

$$p_l = 1, \qquad p_r = 0.1, \tag{4.2}$$

$$\rho_l = 1, \qquad \rho_r = 0.125. \tag{4.3}$$

These states were recreated using a constant number of particles in the left state, and allowing the number of particles in the right state to vary, under the constraint that density $\rho_r = 0.125$. In this way simulation with fewer particles in the right state have a larger mass per particle in that state. 39 simulations were run, and in each case the density profile of the solution was compared to a Riemann solver solution. For each run, the quantity

$$x_i = \sum_j (\rho'_j - \rho_j)^2 \tag{4.4}$$

was calculated for all particles j, where ρ'_j is the density of simulation particle j, and ρ_j is the density at the position of particle j as given by the Riemann

solution. The quantity x_i was calculated for mass ratio i between the particles in the left and right states.

Figure 4.1 shows how x responds to an increasing mass ratio between the particles in the left and right states of the Sod shock tube. In the plot, x has been scaled so that $x_2 = 1$. The mass ratios range from 2 to 60, with the range from 2 to 20 is sampled at intervals of 1. The range from 20 to 60 is sampled in intervals of 2. At a mass ratio of 8, there is a large increase in the relative error of the solution, which is not repeated. However, this may be due to the coarser sampling of the mass ratios larger than 20, so that such localized jumps in x are not resolved. The figure shows that for a mass ratio of less than 20, excluding 8-10, the relative error in producing the Sod shock doesn't increase with the mass ratio. However, the figure as a whole presents an exponential relation between mass ratio and relative error, such that for large mass ratios the error in the solution quickly becomes large.

4.3 The need for an artificial thermal conductivity term

The first detail to be addressed is the ability of standard SPH to solve the point explosion initial conditions using increased resolution in place of thermal conductivity. Particle tests of 32^3 and 64^3 were conducted, to measure the resolution response of Gasoline without a thermal conductivity term. In both runs, the particles are distributed evenly in a cube of dimensions $10 \times 10 \times 10$. The center particle in the cube has an initial energy of $E = 1 \times 10^5$. The background density is $\rho_1 = 1$.

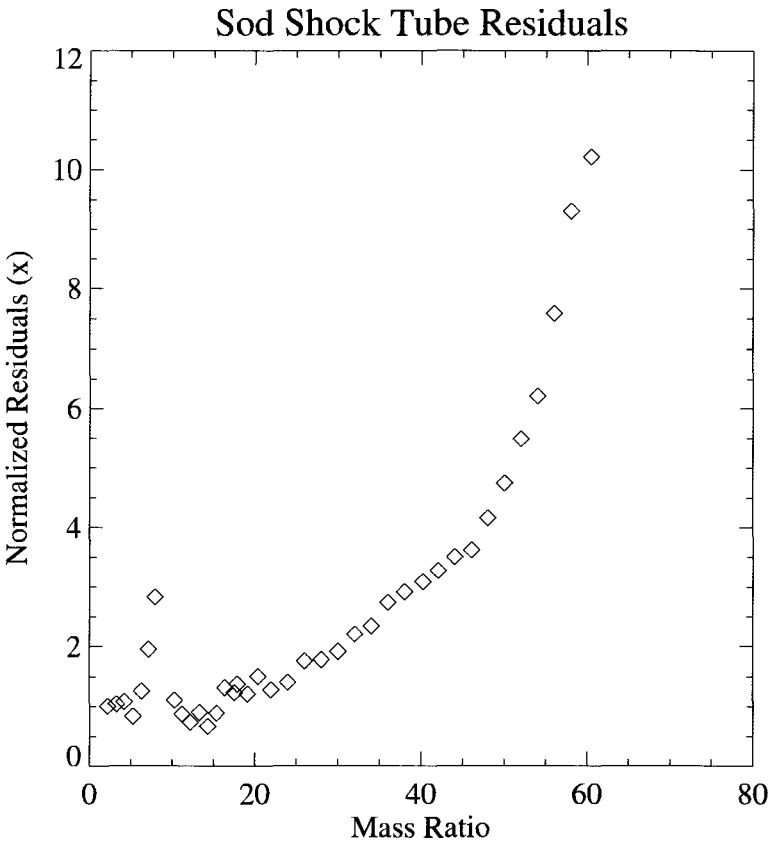

Figure 4.1: Residuals for 39 left-particle-mass to right-particle-mass ratios. The mass ratios range from 2 through to 60. The mass ratio range from 1 to 20 was sampled at intervals of 1, while the range from 20 to 60 was sampled in intervals of 2.

Figure 4.2 shows the cross section of a scatter plot of the particles at four times, $t = 0.025, 0.05, 0.075,$ and 0.1, where the cross section is through the $x - y$ plane, centered at $z = 0$. The first plot shows the initial evolution of a star-like pattern, which develops immediately after the simulation is begun. The six particles which form the nearest neighbors of the central particle into which the blast energy is injected move more quickly than any of the other particles in the simulation, causing them to create the four main spokes visible in the cross section (the other two spokes corresponding to the fifth and sixth particles are perpendicular to the plane of the crossection). A lesser amount of energy is transferred to the eight particles which form the set of next nearest neighbors. The effects of this excess energy can be seen starting from the second plot ($t = 0.05$, in which a secondary set of spokes evolves). While the explosion starts off as a square rotated with respect to the coordinate system, in the last plot ($t = 0.1$) there develops a spherical shock which lags behind the main spokes.

The next figure, 4.3, plots the radial profiles of four fluid quantities, density, pressure, velocity and internal energy. Each profile represents the solution at time $t = 0.1$. The box symbols represent spherical averages over a shell of thickness 0.05, which helps to remove the effects of the asymmetries evident in the scatter plot. The solid black line in each of these plots shows the analytic solution. The first of these plots, the density profile, shows excellent agreement with theory for small radii. At larger radii, however, the solution deviates significantly from the analytic curve. These deviations are the result of inability of the run to predict the correct radius of the shock, with the density peaking at a radius of 4.25 (while the analytic value is 4.59, to three significant

digits). In addition, both the pressure and velocities inside the shock are lower than the analytic solution predicts they should be. The pressure profile can be seen to be qualitatively consistent with the velocity profile, with the lower pressures driving the gas at lower velocities, which in turn is consistent with the shock radius that is smaller than the analytic value. As a tracer of the ratio of pressure to density, the internal energy graph reflects the density and pressure profiles, and in particular the shock front can be seen to be spread across many particle spacings, reflecting the lack of a clear shock boundary in the scatter plot.

Increasing the resolution to a particle count of 64^3 yields the next two plots. Figure 4.4 shows the same cross section of the particle scatter plot (showing the $x - y$ plane centered at $z = 0$). The same pattern of spokes emerges along the directions defined by the nearest and next nearest neighbors of the central particle. The only effect the increased resolution can be seen to have had from these plots is the earlier transition from a cubic shock to a spherical shock behind the most extended spokes at earlier times as compared to figure 4.2. The corresponding radial profiles show that the increased resolution has had no effect on the radius of the shock. The boxes again signify the same spherical shell averaging done in the previous radial profiles, in which each box represents the average value of a quantity over a shell of width 0.05. The solution follows the analytic curve more closely than in figure 4.3, due to the higher peak density value obtained in the higher resolution run. This is consistent with the density smoothing operation performed by SPH, in which shock fronts are spread out over a few particle spacings. With more particles in the shock front, the average particle spacing is decreased, leading to a

better resolved shock with a larger density value. The pressure and velocities qualitatively resemble those for the lower resolution run. The internal energy plot can be seen to follow the analytic curve towards zero much more closely than the same plot with only 32^3 particles, which again shows that the shock front is better resolved with the higher resolution.

Each run had the same blast radius of 4.25 at time $t = 0.1$. Given the complete lack of scaling of the solution radius with resolution, it is clear that increasing the particle count cannot move a version of Gasoline which implements standard SPH towards the analytic solution given in chapter §(3). While no energy is lost in these simulations, the shock front lags behind its predicted value due to the work required to push out the particles in the asymmetric spokes. The time sequence in figures 4.2 and 4.4 shows that the anisotropies have been developing since the earliest stages of the blast.

Table 4.1 gives the run parameters for figures 4.2 - 4.5. Figures 4.3 and 4.5 show the dependence on radius of four fluid variables (density, pressure, velocity, and internal energy). Each box in these plots is a spherical average over a bin of size 0.05. This procedure was used to obtain a single value for the quantities being plotted, as the star-like structure evident in the scatter plots 4.2 and 4.4 would otherwise lead to three radial curves for each variable, one for particles whose radius is at the outer spoke, one for the particles at the outer edge of the spherical shock, and one for the particles at the inner edge (the difference between the last two is most noticeable in the 64^3 run, as is evidenced by its scatter plot).

Table 4.1: Parameters for resolution tests without thermal conductivity

Run Label	Resolution	E	ρ_1
D1	32^3	1.0×10^5	1.0
D2	64^3	1.0×10^5	1.0

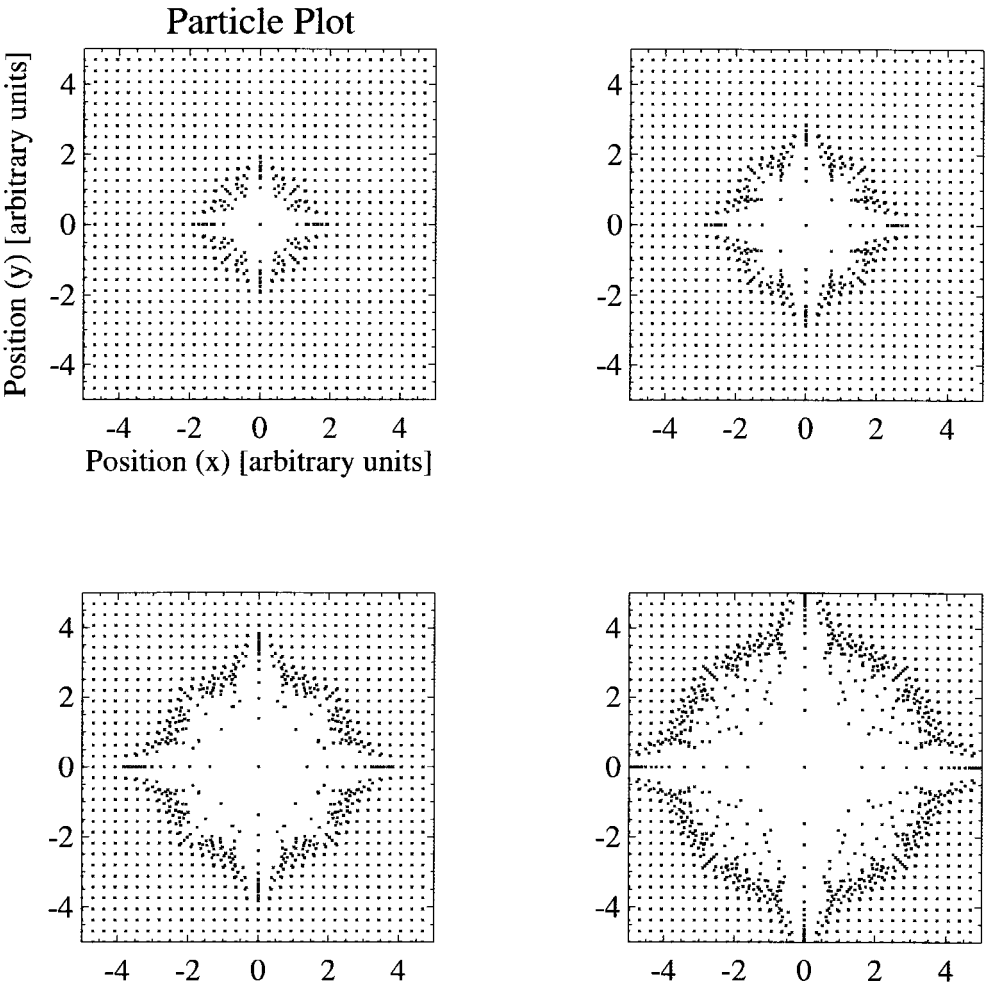

Figure 4.2: Run D1 particle plot sliced through $z = 0$ at $t = 0.025, 0.05, 0.075, 0.1$.

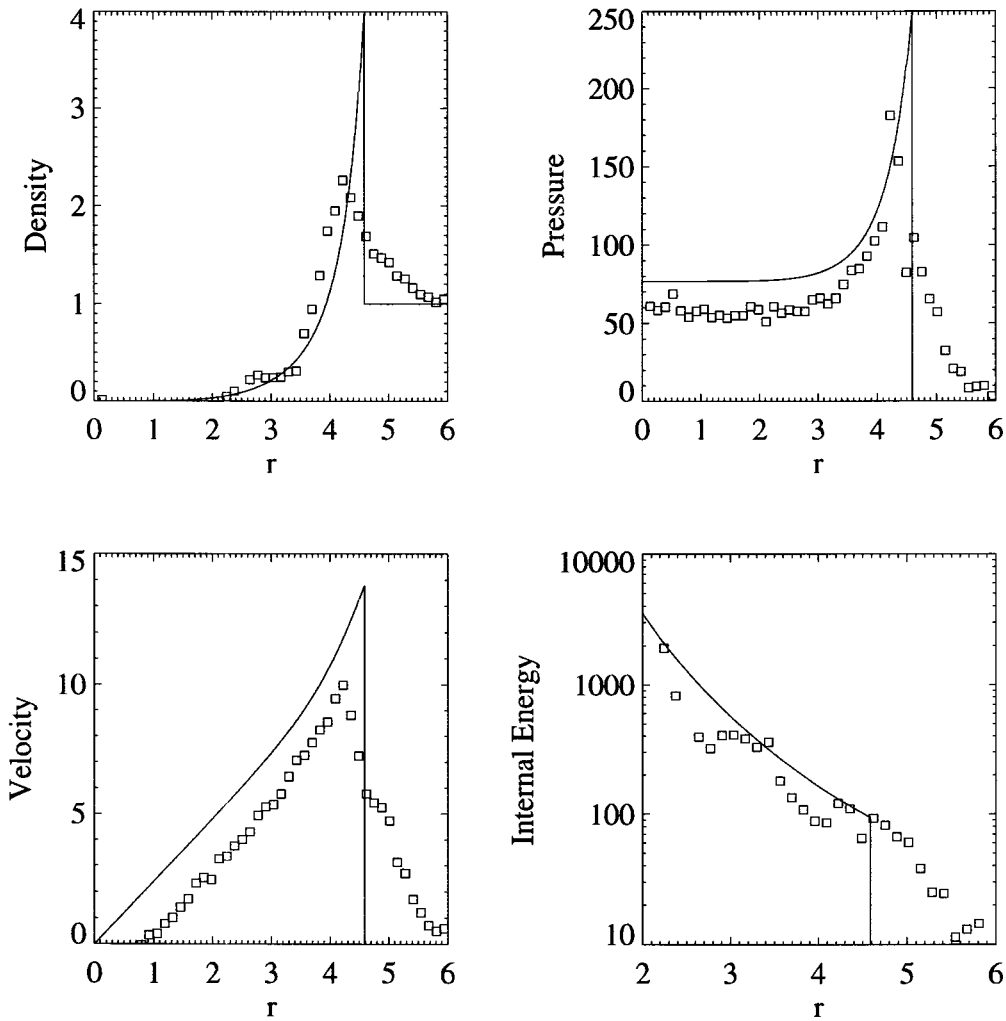

Figure 4.3: Run D1 spherically averaged radial profile plots. Solid lines are the analytic solution curves. Upper left: radial density profile. Upper right: radial pressure profile. Bottom left: radial velocity profile. Bottom right: radial internal energy profile. All profiles are for $t = 0.1$.

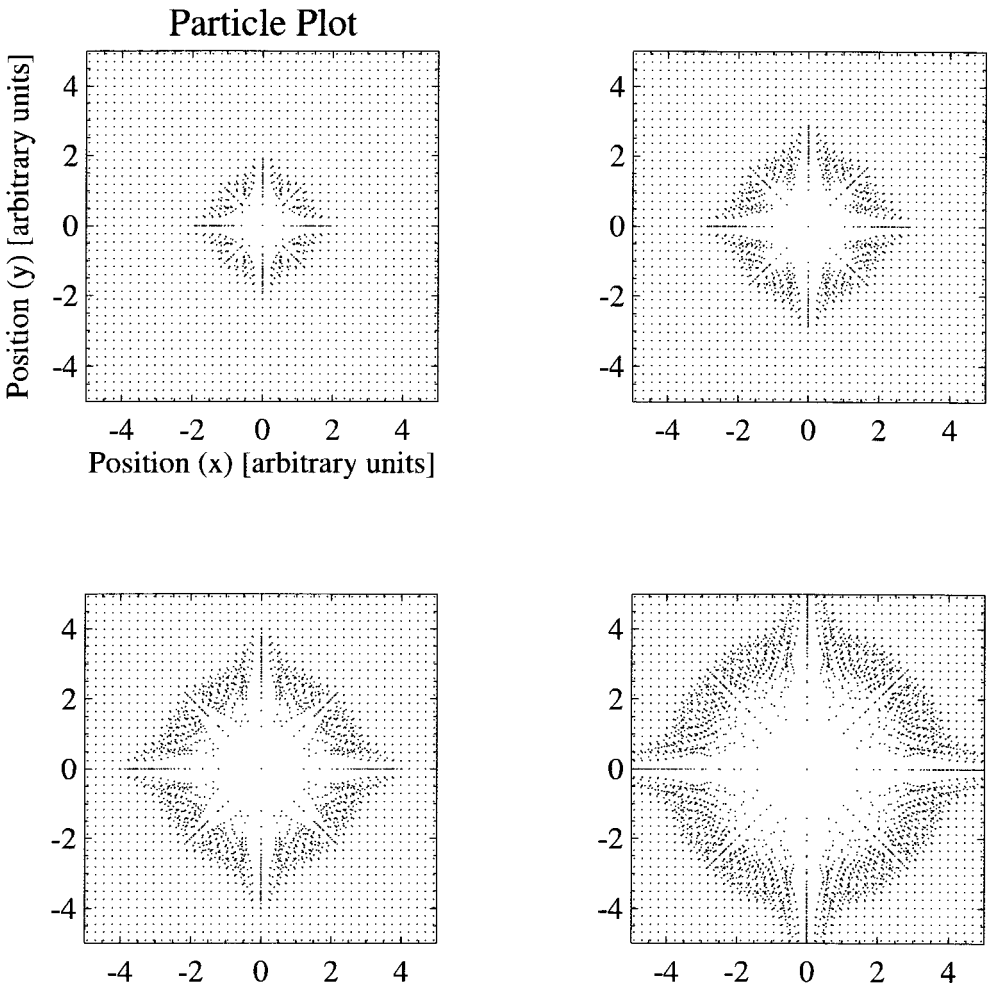

Figure 4.4: Run D2 particle plot sliced through $z = 0$ at $t = 0.025, 0.05, 0.075, 0.1$.

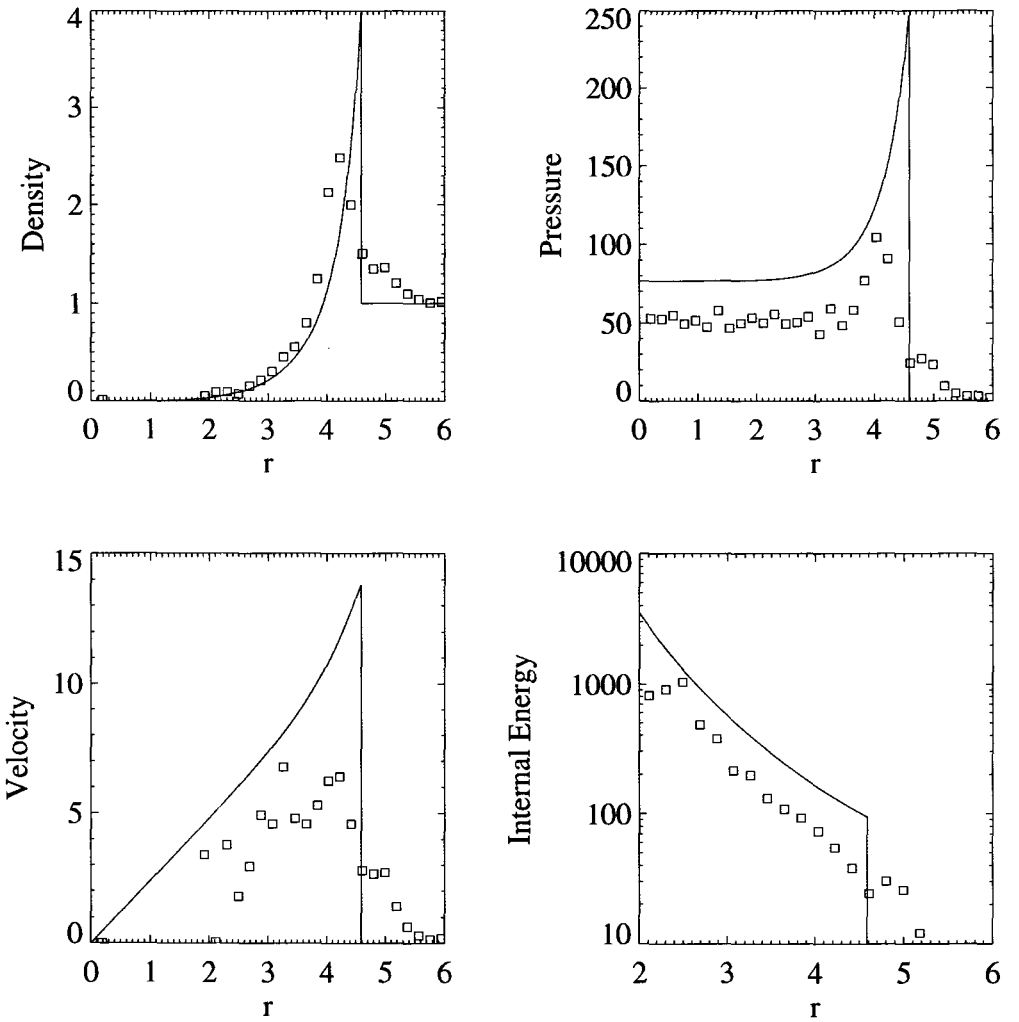

Figure 4.5: Run D2 spherically averaged radial profile plots. Solid lines are the analytic solution curves. Upper left: radial density profile. Upper right: radial pressure profile. Bottom left: radial velocity profile. Bottom right: radial internal energy profile. All profiles are for $t = 0.1$.

4.4 Determining the best overall value of the artificial thermal conductivity parameter, α_u

Since the addition of the thermal conductivity into Gasoline has introduced a new parameter that can be adjusted, its value must be determined. Price & Monaghan (2005) suggested a method for evolving the artificial thermal conductivity parameter α_u, which evolves the parameter according the evolution equation

$$\frac{\mathrm{d}\alpha_u}{\mathrm{d}t} = -\frac{\alpha_u}{\tau} + S, \tag{4.5}$$

where S is a source term given by

$$S = 0.1h|\nabla^2 u|. \tag{4.6}$$

Here, h is the smoothing length, which is multiplied by 0.1 to keep the amount of dissipation small. In addition, there is a maximum value of $\alpha_{u,max} = 1$ which is enforced throughout the evolution. A similar expression is given for the value of α, one of the coefficients of artificial viscosity, but Gasoline implements a constant value for the artificial viscosity coefficient, $\alpha = 1$ and $\beta = 2$. From experience with artificial viscosity, it is unclear as to whether or not the value of α_u must be decided by such an evolution equation, and instead the same approach used for the coefficients of artificial viscosity is used for artificial thermal conductivity: the coefficient is kept constant. We know from the condition imposed on (4.5) that α_u is of order 1, and so we perform several runs of the point explosion problem with varying thermal conductivity coefficients with values consistent with this restriction.

Four runs of the same initial particle conditions were done with α_u taking the values 0.25, 0.50, 1.00, and 2.00. Figure 4.6 shows the evolution of a point

explosion with a thermal conductivity coefficient $\alpha_u = 0.25$. Although the relatively small amount of thermal conductivity has significantly reduced the asymmetry in the scatter plot as compared to figures 4.2 and 4.4, there are still noticeable deviations from spherical symmetry. Increasing α_u to 0.5 and running the same initial conditions yields the time sequence of scatter plots found in figure 4.7. In this test the artifacts visible in runs without thermal conductivity are almost completely gone, although, especially at later times, there are still protrusions extending past the shell of the main shock. These persist for small increments past a value of $\alpha_u = 0.5$, and in fact it isn't until a value of $\alpha_u = 1$ that these finally disappear. The scatter plot of the particles in the run with a thermal conductivity coefficient of 1 is shown in figure 4.8. The defects of the runs with smaller thermal conductivity coefficients are drastically reduced, but more importantly they do not become more prominent as the simulation progresses, unlike the runs with $\alpha_u = 0.25$ and 0.5. As a test of further progressions of α_u to higher values, figure 4.9 shows the evolution of a point explosion with a thermal conductivity coefficient of 2. As with $\alpha_u = 1$, the defects do not grow larger with increasing time, but neither does the simulation have any remarkable qualitative difference from the one with a coefficient of 1.

From figures 4.6 – 4.9, the minimal value of α_u which adequately recovers the spherical solution is 1, which is the value used for all further runs with artificial thermal conductivity.

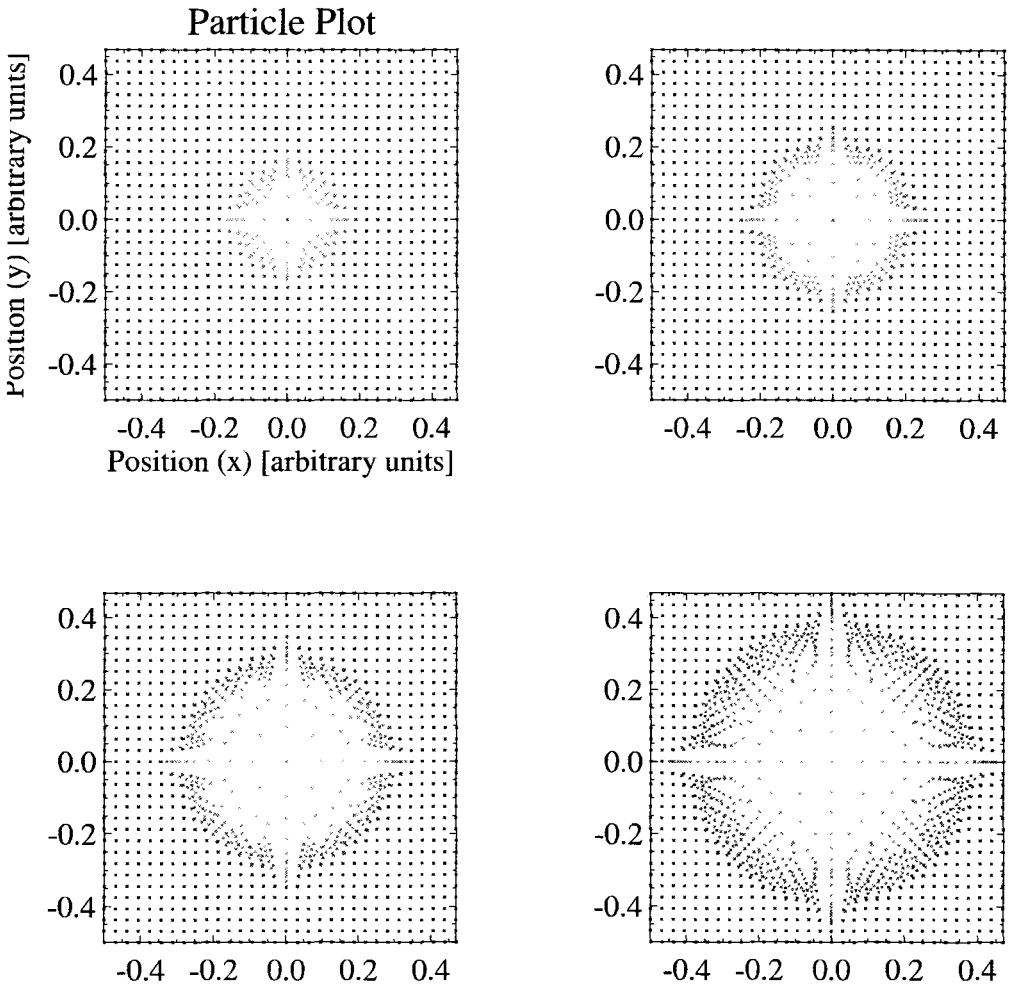

Figure 4.6: Results of a gridded particle, point explosion simulation with Gasoline with thermal conductivity, with a thermal conductivity coefficient $\alpha_u = 0.25$.

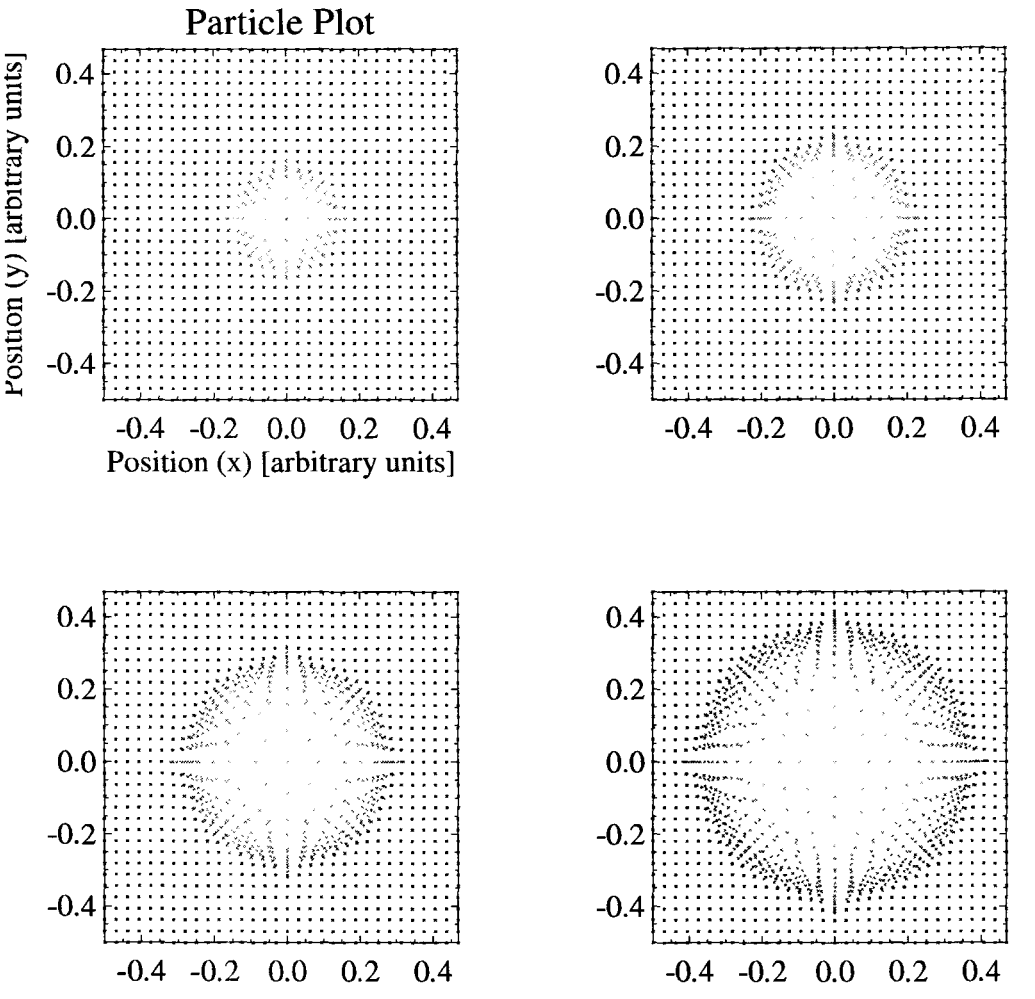

Figure 4.7: Results of a gridded particle, point explosion simulation with Gasoline with thermal conductivity, with a thermal conductivity coefficient $\alpha_u = 0.50$.

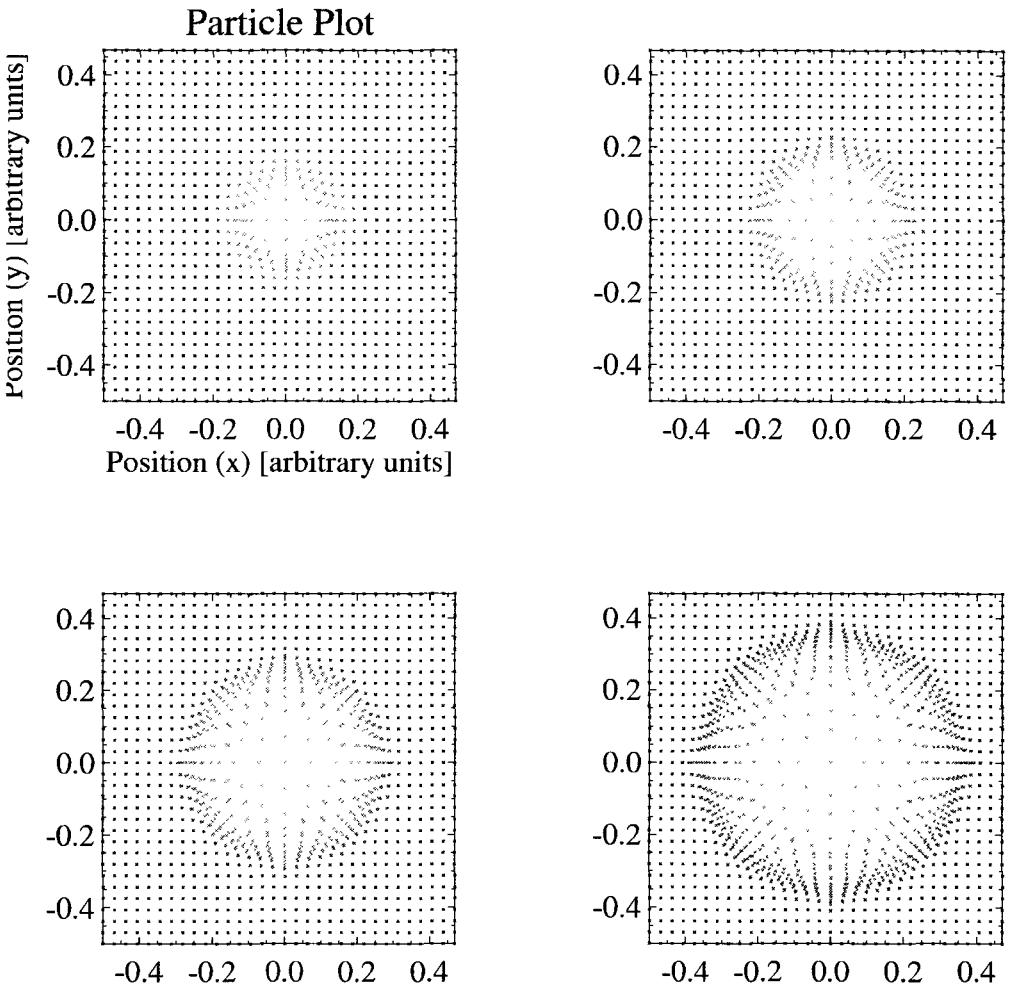

Figure 4.8: Results of a gridded particle, point explosion simulation with Gasoline with thermal conductivity, with a thermal conductivity coefficient $\alpha_u = 1$.

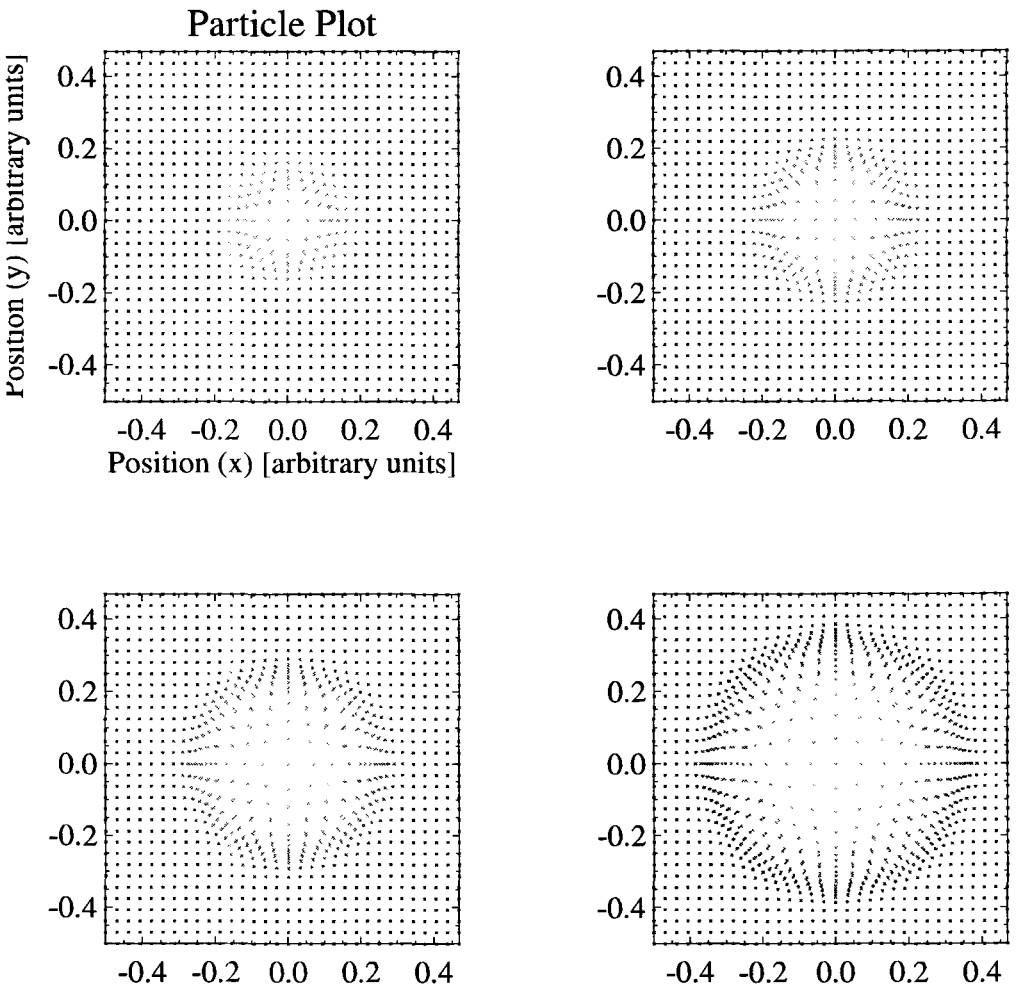

Figure 4.9: Results of a gridded particle, point explosion simulation with Gasoline with thermal conductivity, with a thermal conductivity coefficient $\alpha_u = 2$.

Table 4.2: Parameters for resolution tests with thermal conductivity

Run Label	Resolution	E	ρ_1	α_u
TC1	64^3	1.0×10^5	1.0	1
TC2	32^3	1.0×10^5	1.0	1
TC3	16^3	1.0×10^5	1.0	1

4.5 Resolution sensitivity of the application of artificial thermal conductivity

The scientific validity of any method is dependent upon the repeatability of the results. In numerical methods, one necessary condition on the behavior of a code or algorithm such that it is reproducible is that it must converge to a solution as resolution is increased. If this can be shown to be true, it is also nice to test the lower bounds on the resolution such that the solution arrived at is still suitably accurate, with the hope that introducing new algorithms won't increase the overall need for resolution in a code.

All runs in this section have a central particle with energy $E = 1 \times 10^5$, embedded in an ambient density of $\rho_1 = 1$. The simulation box size is $10 \times 10 \times 10$. The simulation parameters for each run are given in table 4.2.

Figure 4.10 presents the scatter plot of run TC1, and in figure 4.11 are the radial profiles for the last bottom right scatter plot in figure 4.10. The radial density plot has a maximum value of 2.25, compared to the analytic maximum density contrast of four between the post-shock density and background density. Despite the low peak density, this result is encouraging when compared the peak density of the run TC2 with a resolution of 32^3 particles: in this run, the peak density is 1.9 for the same time, so that increasing the resolution of a simulation brings it closer to the analytic value. A similar analysis holds

true for the density in the middle of the shock, which is elevated above the analytic value, though not so much as in the case of lower resolution. The radius of the shock matches extremely well with the analytic solution, and immediately after the the shock the density profile falls off parallel to the analytic solution, though the simulated and predicted curves do overlay one another, as a consequence of the smaller peak density in the simulated curve. Shortly after the shock, the slope of the simulated density curve can be seen to differ from the analytic solution, so that the simulated density curve, which is initially underneath the analytic curve, crosses over and then remains above the analytic curve as r goes to zero. For the simulations run for this thesis, the excess density doesn't pose much of a concern, and as already mentioned, the central density can be made as small as desired with increased resolution. However, in a more elaborate simulation which includes cooling, the elevated density with the high temperatures that remain in the core of the supernova remnant could lead to artificially high cooling rates which negatively impact the accuracy of the results. Such tests are a good direction for future work.

The pressure curve in figure 4.11 mirrors the excellent placement of the shock radius seen in the density profile, and on average the post shock pressure curve follows the analytic curve as r goes to zero. There is however a ringing of the pressure after the shock, which is also identified in Rosswog & Price (2007), and seems to be the lasting effects of initiating the blast in a gridded initial particle distribution. The velocity profile gives good agreement with the Sedov-Taylor solution, while the internal energy profile reflects the density and pressure plots, from which it can be constructed as a ratio of pressure to density. The elevated density as r goes to zero is reflected in the internal

energy profile where the simulation curve falls below the analytic value in the same region of radius. At the same radius where the simulated density curve crosses the analytic one, the simulated internal energy curve crosses its exact counterpart, with a slight oscillation reflecting the post shock ringing in the pressure profile. The last feature of the simulated internal energy, the final increase before falling off to zero, replicates the small peak density at the shock radius.

Next are the results of run TC2, with a resolution of 32^3 particles. The decrease in density has no effect on the radius of the shock, which remains true to the analytic value of 4.59. The peak density is decreased somewhat compared to run TC1, with a maximum value of 1.9. The same general comments about the form of the density curve compared to that of the analytic solution can be applied to this run, where the slope immediately behind the shock matches well with the analytic solution, but for radii smaller than about four, the slope becomes noticeably smaller than predicted. Despite this discrepancy, the pressure curve approximates the exact solution well, with only a slightly higher slope post-shock as compared the Sedov-Taylor solution. With the decrease in resolution, it becomes hard to tell if the solution has the same post shock oscillations as in run TC1, or simply a large pressure spread at the same range of radii. The average velocity profile follows the analytic curve closely, though the characteristic noise of velocity measurements in SPH causes a lot of scatter about either side of the exact solution. Once again the features of the density profile can be seen mirrored in a different form in the internal energy profile.

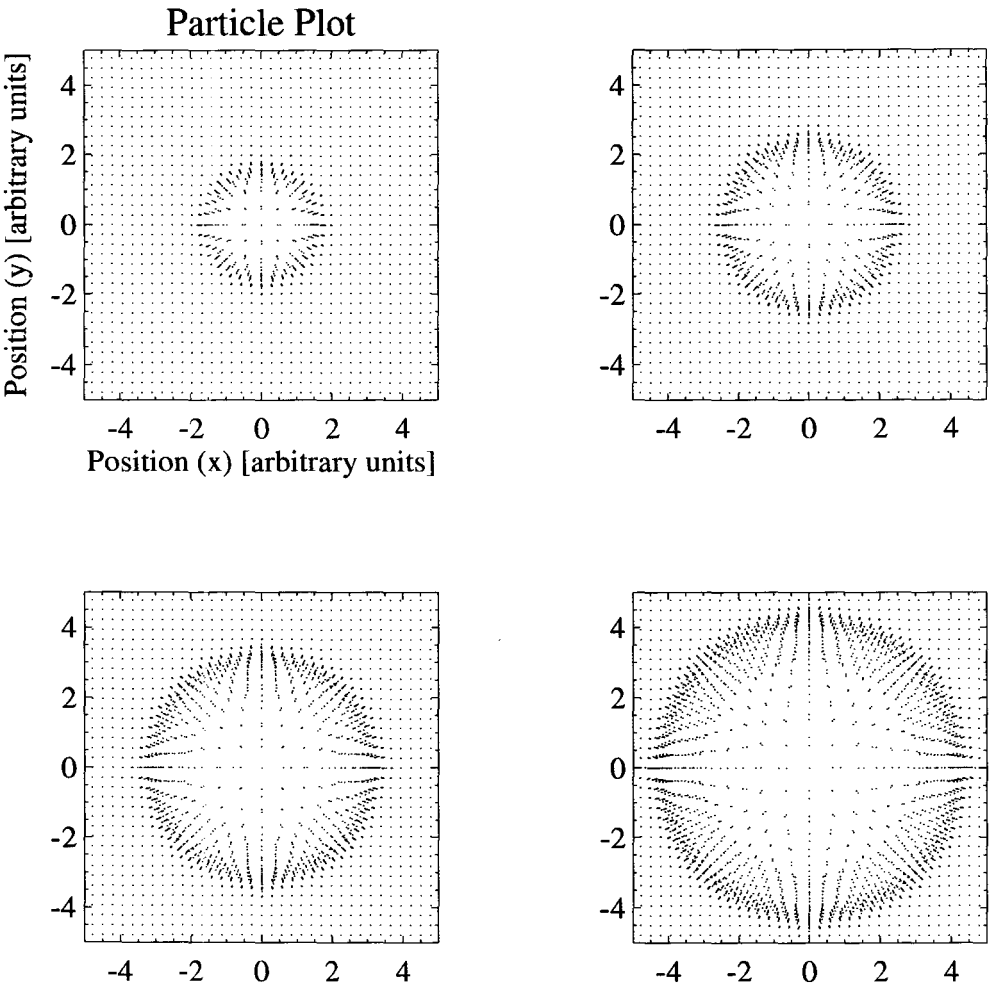

Figure 4.10: Run TC1 particle plot sliced through $z = 0$ at $t = 0.025, 0.05, 0.075, 0.1$.

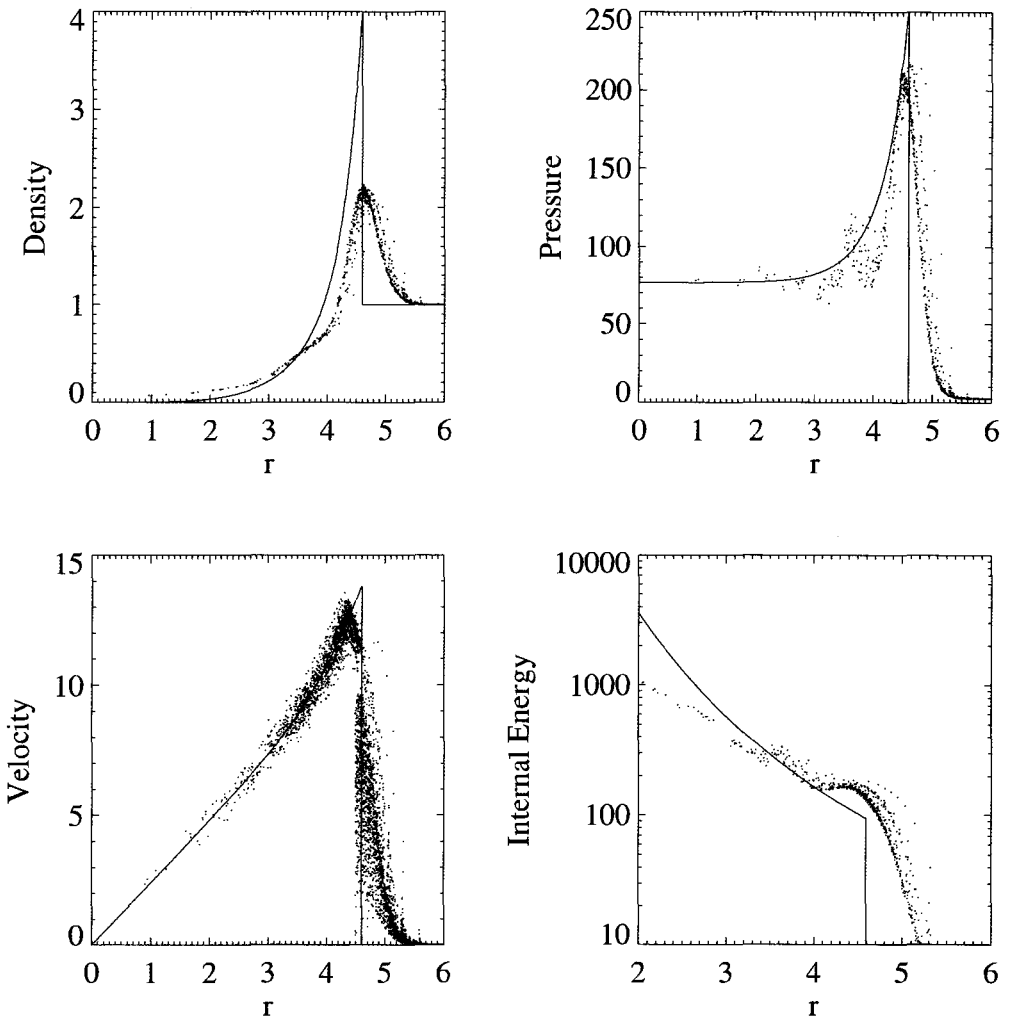

Figure 4.11: Run TC1 radial profile plots. Solid lines are the analytic solution curves. Upper left: radial density profile. Upper right: radial pressure profile. Bottom left: radial velocity profile. Bottom right: radial internal energy profile. All profiles are for $t = 0.1$.

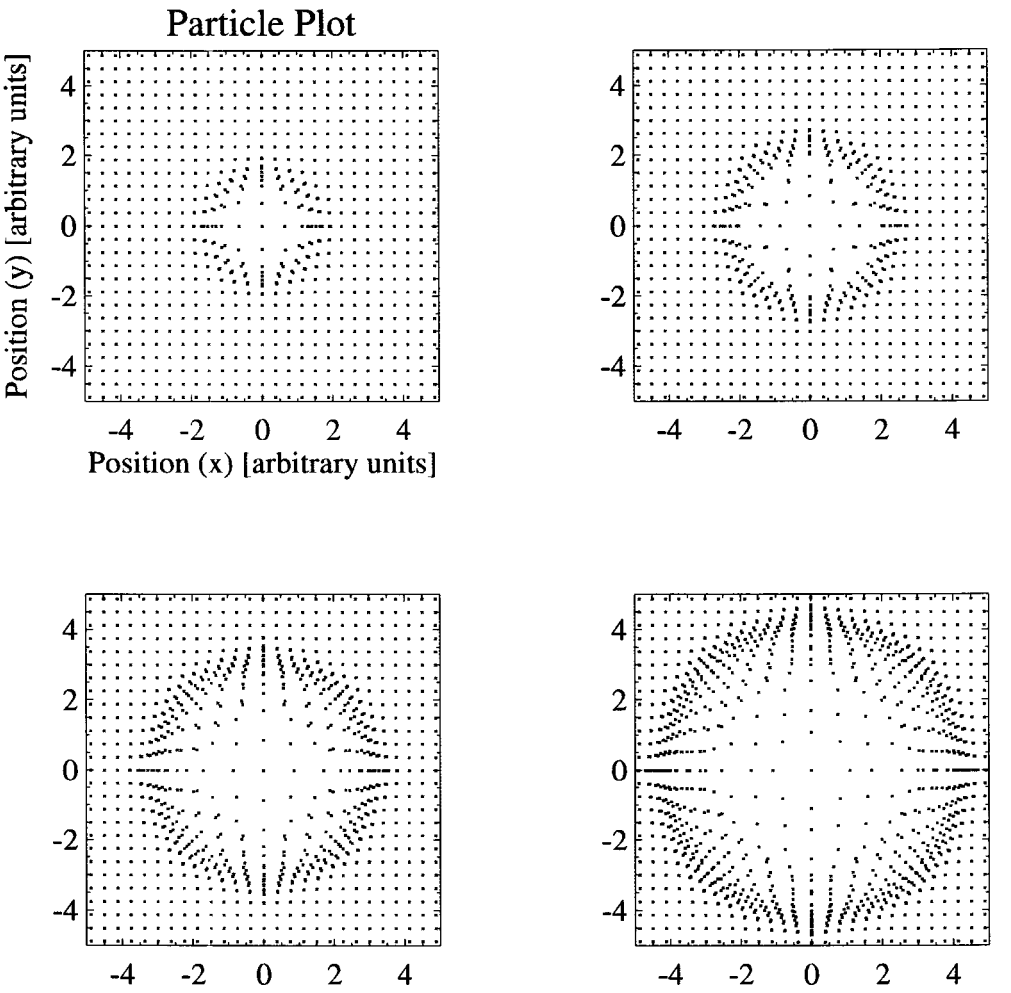

Figure 4.12: Run TC2 particle plot sliced through $z = 0$ at $t = 0.025, 0.05, 0.075, 0.1$.

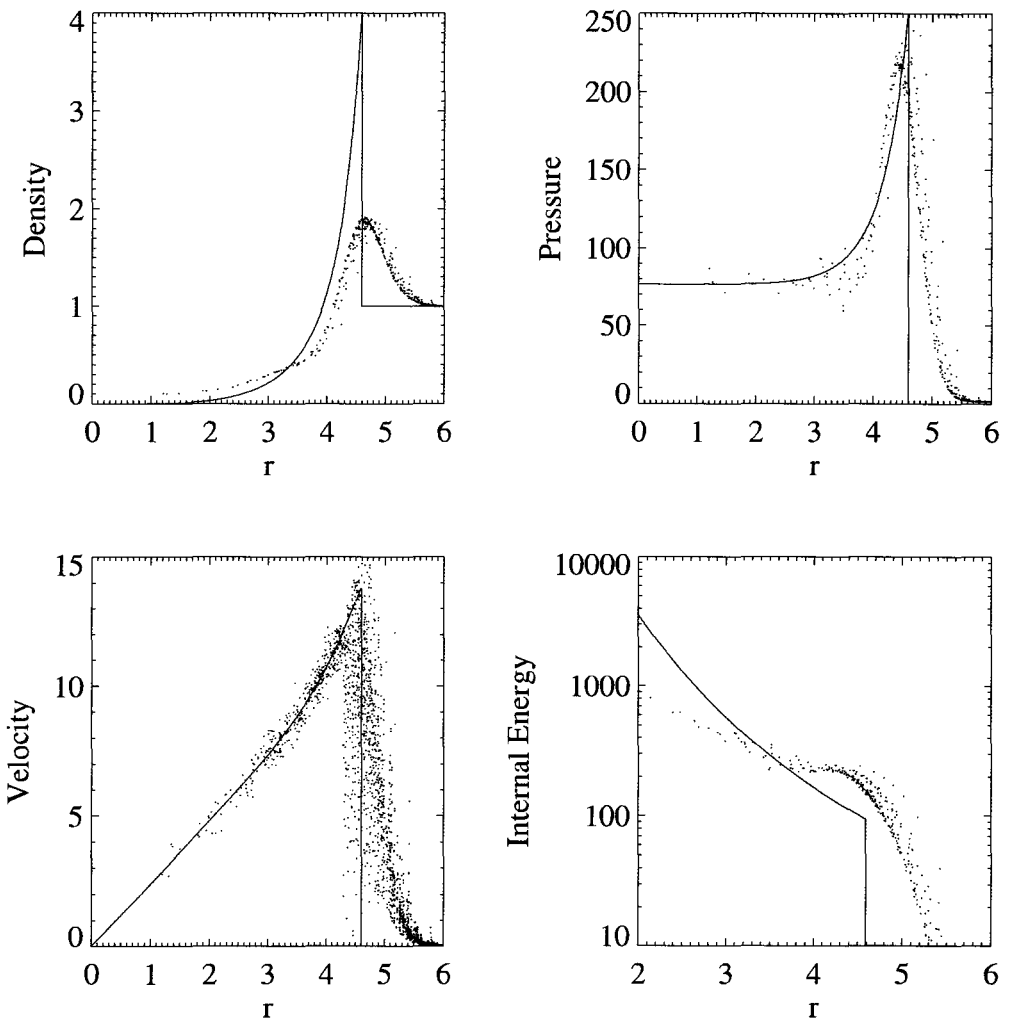

Figure 4.13: Run TC2 radial profile plots. Solid lines are the analytic solution curves. Upper left: radial density profile. Upper right: radial pressure profile. Bottom left: radial velocity profile. Bottom right: radial internal energy profile. All profiles are for $t = 0.1$.

The last run is labeled TC3, has a resolution of only 16^3. Figure 4.14 demonstrates that some of the spherical symmetry present in the solution with resolutions of 32^3 and 64^3 is lost with such a low particle count. However, the density profile in figure 4.15 shows that despite the lack of symmetry, the radius of the shock still matches the analytic value of 4.59. The other radial profiles suffer from a large amount of noise compared to the number of particles there are, making the pressure profile in particular hard to evaluate. The velocity profile is characteristically accurate, if not particularly precise.

4.5.1 Summary of Resolution Tests

Table 4.2 gives the resolution values for three runs reported in figures 4.10 - 4.15. Note that, in contrast to figures 4.2 - 4.5, no averaging has been done to create these plots. the point plotted represent individual particles. The three runs show that the radius of the shock is reproduced for all resolutions, so by that measure resolution has a negligible effect on the ability of a thermal conductivity term to operate. Fortunately, the peak density does not remain constant, nor does the minimum density that is approached as the radius goes to zero. For a run with 32^3 particles, the peak density has attained a value of 1.9 at t=0.1, whereas the run with 64^3 particles has a peak density of 2.25 for the same time, demonstrating that with larger resolutions the highest density jump possible will be obtained. Also, since the number of particles that are present in the shock increases with time, the peak density value in the shock will tend towards the limit of $\rho_{shocked}/\rho_{unshocked} = 4$.

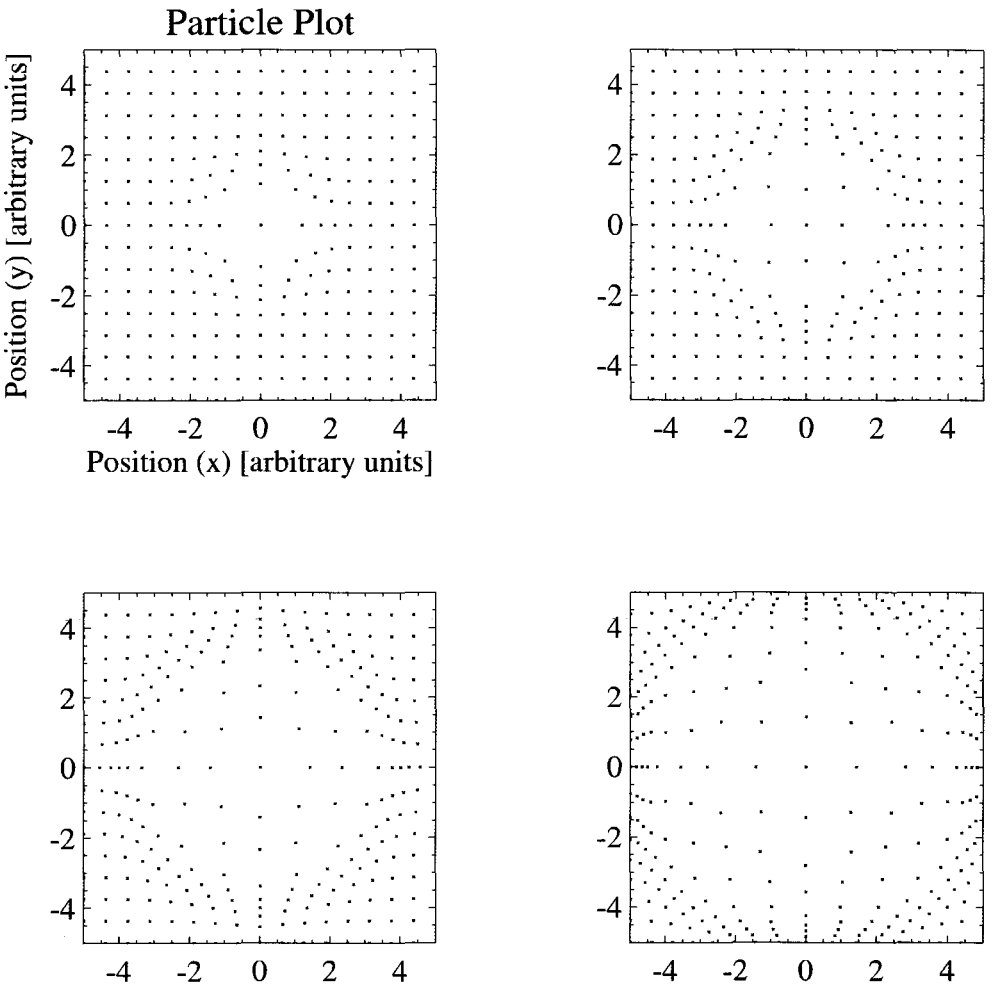

Figure 4.14: Run TC3 particles plot sliced through $z = 0$ at $t = 0.025, 0.05, 0.075, 0.1$.

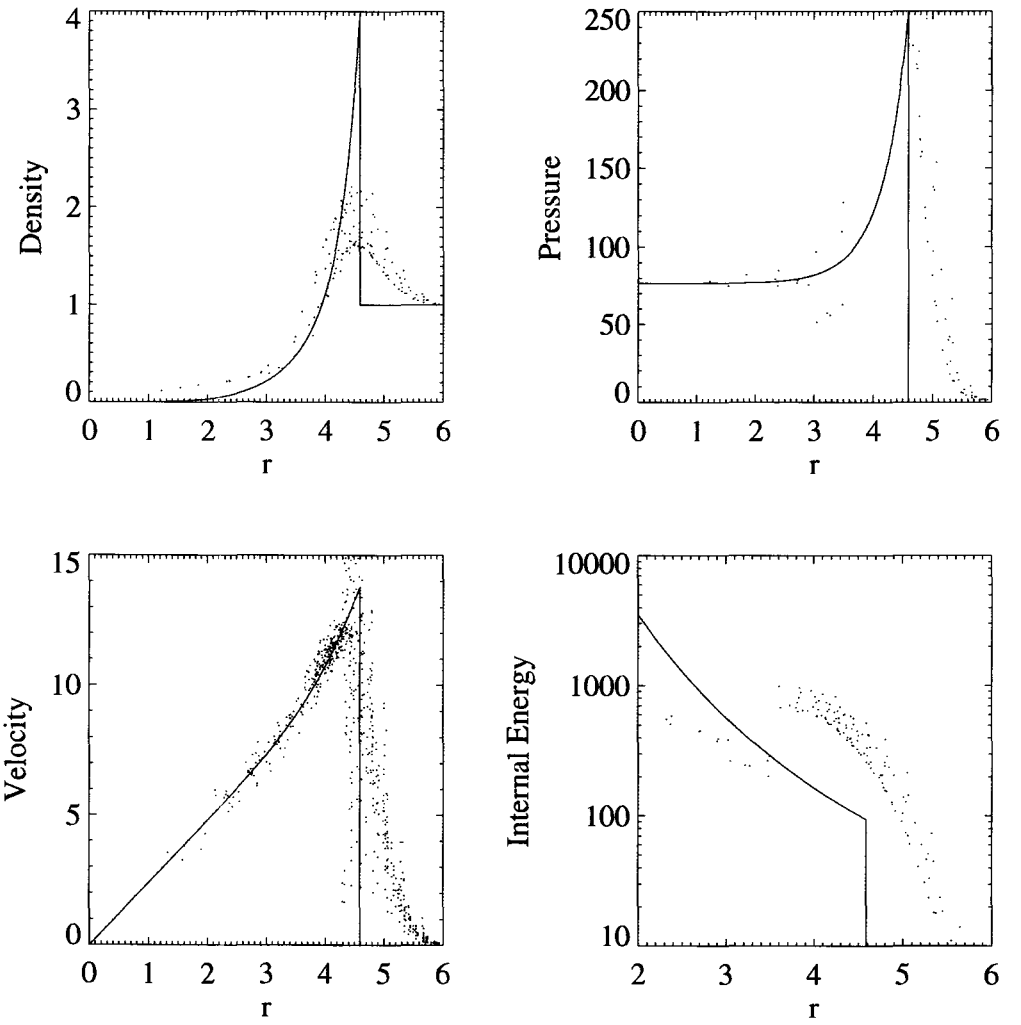

Figure 4.15: Run TC3 radial profile plots. Solid lines are the analytic solution curves. Upper left: radial density profile. Upper right: radial pressure profile. Bottom left: radial velocity profile. Bottom right: radial internal energy profile. All profiles are for $t = 0.1$.

Similar in behavior to the peak density in the shock, the limiting density value in the middle of the interior drops with increasing resolution, so that here too the solution can be expected to tend to the analytic curve with increasing resolution.

Although it is impressive that the 16^3 run was able to reproduce the radius of the shock, the particle scatter and significant errors in the pressure profile, in particular, indicate that such low resolutions are at the floor of what would be required to resolve a supernova explosion in a real simulation.

The internal energy plots should be interpreted as reinterpreting the same information that is available in the density and pressure profiles, an in particular the departures of the internal energy plots from the analytic solution only reflect the errors in either the density profile or the pressure profile. Since the pressure profiles are quite good for both runs TC1 and TC2, the errors in the internal energy are attributable to the overdensity in the middle of the solution (which tends to incorrectly lower the internal energy near $r = 0$), and the low peak density at the shock (which raises the internal energy at that radius).

4.6 Stepping away from grid initial configurations

Looking in detail as to how the anisotropies develop in the runs using gridded particles as an initial condition, the first time step of any run reveals that energy is preferentially being distributed to the six particles that are the nearest neighbors of the detonation particle. As a test to see what happens if the particles are arranged in a disordered state, so that there are no directions defined by the chaining of nearest neighbor vectors, a run was set up to mimic the tests performed above, but with the particles arranged as a glass, rather than grid, configuration. The particles are settled into their glassy state by evolving an initial grid configuration of particles with a energy operator that removes 20% of the particle's velocity every time step, so that the particles move into their equilibrium position and then their velocities are killed off, leaving them in a stable state where the there are no preferred directions for finding nearest neightbours.

The resolution is set to be the same as that of run TC2, that is there are 32^3 particles, and the source particle is given the same amount of initial energy, $E = 10^5$. The background density has an average value of $\rho_1 = 1$, and the simulation box size is $10 \times 10 \times 10$. The profiles reported in figure 4.16 have values which have been spherically averaged as, despite the accuracy of the results, there was a lot of noise in the raw particle plots. Each value is averaged over a radial bin of size 0.05. The profiles were taken at time $t = 0.1$. No thermal conductivity was used.

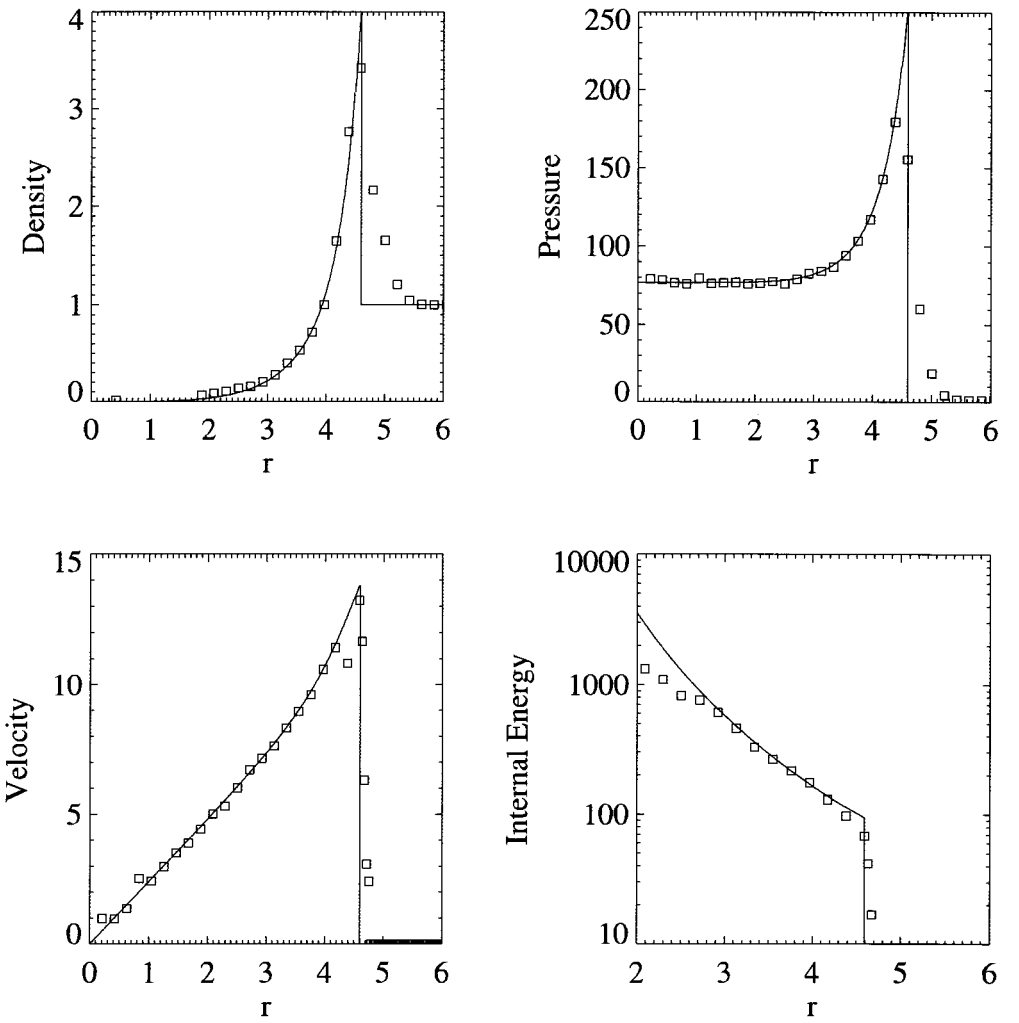

Figure 4.16: Gasoline run using a glass initial condition, without any thermal conductivity. The input energy $E = 10^5$ as in previous tests. All profiles are for $t = 0.1$.

The density profile matches the Sedov-Taylor analytic curve down to a radius of approximately 3, where it starts to become elevated by about 0.1. This is reflected in the internal energy plot, where for radii smaller than 3, the simulation values start to fall below the analytic curves. At the shock front, for which the shock radius is captured well by the simulation, the peak density is 3.45, slightly less than 14% lower than the maximum value of 4. The pressure profile shows that the simulation results and analytic curve agree up until the the shock front is met, where the peak pressure is only 182, instead of the 250 that is predicted. The velocity profile recreates the analytic velocity curve well, with increasing variance at small radiance and near the shock. Also, when the particle noise is averaged out, the shock is captured with a comparitively compact width.

4.7 Detonations in an exponential atmosphere

The last type of simulation that was performed was a blast going off in an exponential atmosphere, the analytics of which were presented in §(2.3). Since this problem must now worry about gravitational effects, the solution isn't dimensionless. In figure 4.17, the unit of length is 100 pc, and the solution is presented after 1.5 Myr. The initial energy is $1.41 \times 10^{51} erg$, and the scale height of the atmosphere is 100 pc, so that there are three scale heights from the bottom of the box to the top. These values allow for a comparison to made to the work of Stil et al. (2008), who used ZEUS-MP (Norman, 2000) to look at the bubble blown out by a more continuous energy injection. While figures 4.17 and 4.18 allow only qualitative comparisons, they appear to agree well with each other. A better test of the Gasoline run is the semi-minor to semi-major axis ratio of the bubble when $a = 1.7h$, which is $b/a = 0.88$, only 2% off its analytic value of 0.9 at that time (Maciejewski & Cox, 1999).

For the very late evolution of the supernova in the exponential atmosphere, Figure 4.19 shows the scatter plot of the blast wave. The figure is shown at a time $t = 20 Myr$. The blast wave extending perpendicular to the density gradient expands 30% beyond the value given by the Kompaneets solution, however in contrast to the semi-minor axis, the semi-major axis only 3% less than the expected analytic value.

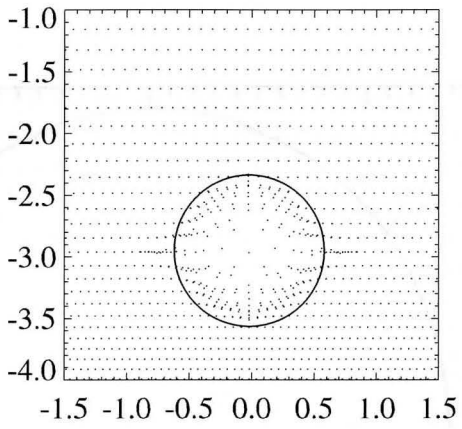

Figure 4.17: Detonation in an exponential atmosphere. The unit of distance on the figure is 100 pc.

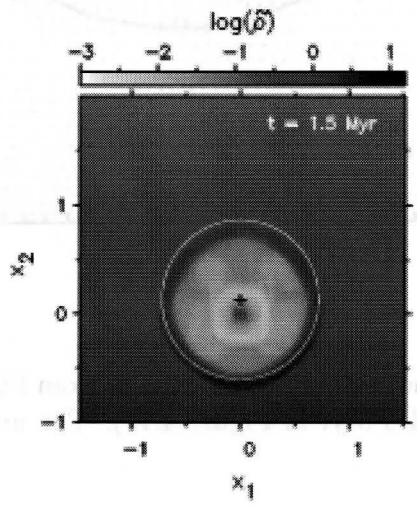

Figure 4.18: An analogous simulation run by Stil et al. (2008)

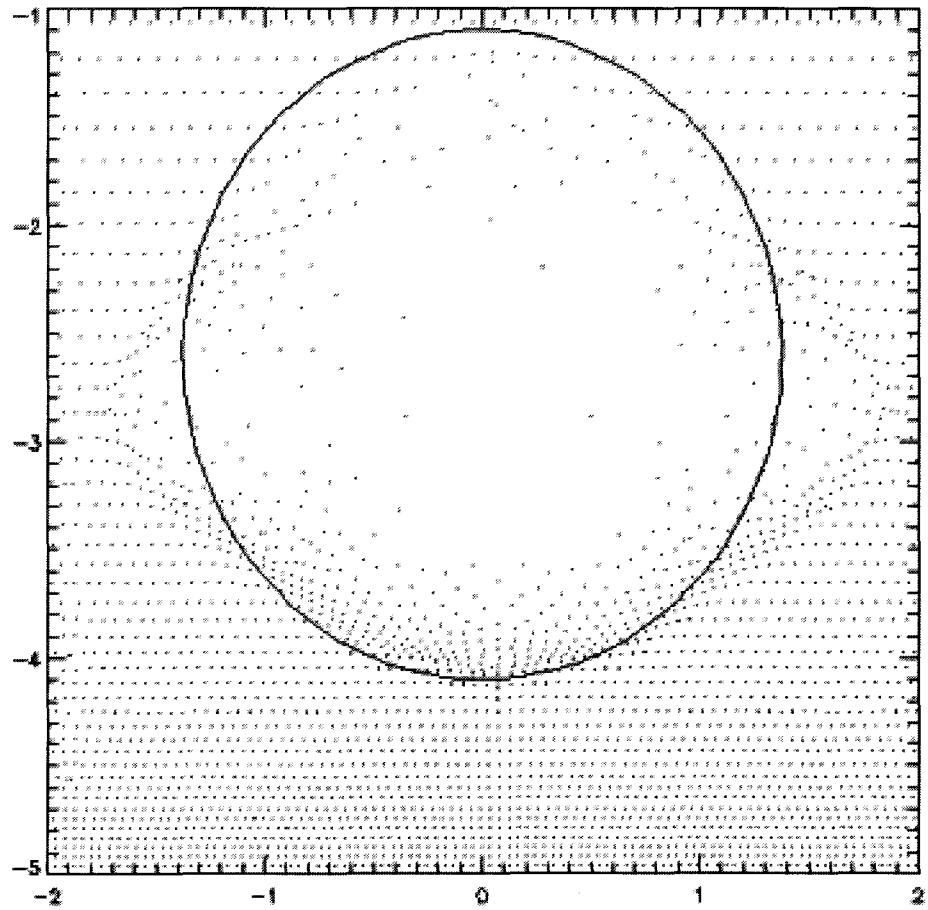

Figure 4.19: The supernova bubble that evolves from Figure 4.17. The time is 20 Myr (as opposed to 1.5 Myr in Figure 4.17). The unit of distance is again 100 pc.

4.8 Discussion

When a large amount of energy is given to single SPH particle in a gridded particle distribution, the standard equations of SPH are unable to reproduce the Sedov-Taylor blast wave solution that describes just such a detonation. The inability to simulate the blast radius is independent of the resolution used to simulate the explosion, and so for the special case where the particles are arranged in a grid and all of the explosion energy is given to one particle, the introduction of a artificial thermal conductivity term is required.

In introducing the artificial thermal conductivity into the SPH equations, an additional free parameter becomes available, and it is assumed, through analogy to the coefficients of artificial viscosity, that this parameter can be taken as constant. In the Sedov-Taylor blast wave problem, the value for the thermal conductivity coefficient α_u that best simulates the analytic solution is 1. In testing with three different resolutions as well as with an exponential atmosphere explosion, the assumption that α_u can be held constant is upheld, and no change to this parameter is found to be needed.

The artificial thermal conductivity term introduced into the SPH equations solved by Gasoline allows for the problem of the blast wave resulting from the injection of a large amount of energy into a single SPH particle amongst a grid of particles to be accurately simulated with respect to the radius of the shock wave. Tests at various resolutions show that the radius of the resulting shock wave at a certain time is independent of the resolution used in the simulation. However, the peak density achieved at the shock front, was well as the density in the center of the explosion do depend on the number of particles

used, with increasing resolution leading to a better value for both the peak shock density and the central remnant density. Since the number of particles that are caught up in the shock increases as the shock propagates through the background medium, the peak density of the shock increases towards its limiting value as time increases.

A more physically interesting test is that of the detonation in an exponential atmosphere, where the inclusion of the thermal conductivity term into Gasoline was required for the successful simulation of a blast wave given by Kompaneets' solution at early times. In addition to agreeing with the Kompaneets' solution after 1.5 Myr, the test agreed with work done by Stil et al. (2008), whose simulations were done with the grid code ZEUS-MP.

Evolving the detonation in the exponential atmosphere further, the semi-major axis of the blast wave followed Komapaneets' solution to within 3% up to 20 Myr, after which the blast wave escapes the atmosphere and its evolution could not be followed further. However, the semi-minor axis shows considerable deviations away from the analytic value (30%), with the largest discrepancy occuring at the height of the original detonation.

The need for an artificial thermal conductivity term is not universal however: using an initial condition in which the particles are not forced into a gridded initial state, but are instead allowed to relax into a glass state, leads to a Sedov-Taylor blast wave solution when the initial energy is deposited into a single particle, but no thermal conductivity is used. This result is encouraging for cosmological simulations, in which the particles never find themselves

back in a gridded structure in high density regions once the simulation has started.

Of the three key features of the blast wave solution (density, temperature, which is directly related to the energy in these adiabatic explosions, and radius), only the radius of the blast consistently matches the Sedov-Taylor solution for the runs with gridded particles and no smoothing of the injection energy. However, with the artificial thermal conductivity term, the density and internal energy can be made increasingly accurate with increasing resolution.

Chapter 5

Conclusion

A method for resolving discontinuities in the thermal energy of a flow has been introduced in the Gasoline code. With this artificial thermal conductivity term, an initial condition in which a single particle was given a large amount of energy and placed in the middle of a grid of relatively pressureless gas particles can be evolved to form a solution with both properties that are independent of resolution and properties that converge with increasing resolution. The expected solution to this scenario is the Sedov-Taylor blast wave, and this solution is recovered with varying degrees of success. In comparison to the case where the code is run without artificial thermal conductivity, the evolution of the initial conditions described above shows a noticeable difference in all aspects, from the visible symmetry of the solution to the radial profile of the flow variable pressure, density, velocity, and internal energy.

For the initial particle setup that has all the particles on a grid, the results of Gasoline with thermal conductivity are measurably closer to the Sedov-Taylor solution than the results without. The evolution of the blast radius with time shows excellent agreement with theory, and it is an agreement that doesn't depend on the resolution of the simulation. Other measures with which

to compare the analytic solution and the simulated one, such as the density at the shock or the density behind the shock in the center of the remnant show that the numerical solution does not agree completely with the Sedov-Taylor solution, but that these discrepancies decrease with increased resolution, so that the numerical goal of convergence is achieved.

The elevated density in the core of the remnant suggests an interesting avenue for further work, which is to run the test with a cooling function activated in the code. This would allow for the determination of how much the excess density would affect the ability of the supernova remnant to expand out into the surrounding medium, and if the cooling of the overdense gas would be enough of a drain on the energy sustaining the expansion of the supernova's bubble to cause it to cease its Sedov-Taylor like evolution before it otherwise would.

When the particles where not initially arranged on a grid, but instead allowed to relax into a glass configuration, the need for an artificial thermal conductivity term was seen to disappear. This result is a confirmation of the long observed behavior of SPH simulations to be able to more easily simulate a process when the particles are allowed to reach this glassy state, rather than being set up on a grid. The test of a detonation in an exponential atmosphere compared favorably to both the analytic solution given by Komapaneets, as well as the work of another numerical group (Stil et al., 2008) working with a grid based code, ZEUS-MP.

The need for artificial thermal conductivity should be recognized as being limited in terms of the type of problem that requires such a modification to the

SPH equations. In runs where there is sufficient resolution to model the blast energy as being distributed over the neighbors of the source particle, Gasoline and SPH in general produce simulation results which match the Sedov-Taylor solution, regardless of the initial particle distribution. For particles which are allowed to relax to form a glass before the energy is injected into the simulation, standard SPH is again able to match the analytic solution. However, for a simulation run with particles initially on a grid, and with the blast energy concentrated in one particle, standard SPH fails to recreate the Sedov-Taylor solution. The interest in such a case comes from the desire to have an sub-grid processes captured accurately in terms of its effects on processes that are resolved. With artificial thermal conductivity, point-like energy feedback in a set of gridded particles can be accurately modeled.

In his paper, Price (2008) argues that 'The need for such an artificial thermal conductivity contribution in order to resolve discontinuities in thermal energy is almost universally ignored in SPH formulations.' However the work done in this thesis makes a weaker conclusion as to the necessity of the artificial thermal conductivity term: in simulations of a point-like explosion, such a term is only necessary when the initial particle configuration is a grid, and where the blast energy is initially confined to a single SPH particle. For such an initial condition, the blast radius given by the Sedov-Taylor solution is recovered, while the density and internal energy profiles are limited in accuracy by the resolution of the simulation.

Bibliography

Agertz, O., Moore, B., Stadel, J., Potter, D., Miniati, F., Read, J., Mayer, L., Gawryszczak, A., Kravtsov, A., Nordlund, A., Pearce, F., Quilis, V., Rudd, D., Springel, V., Stone, J., Tasker, E., Teyssier, R., Wadsley, J., & Walder. 2007, MNRAS, 380, 963

Begelman, M. C. 1985, ApJ, 297, 492

—. 2003, arXiv:astro-ph/0303040v1 [astro-ph]

Begelman, M. C. & Cioffi, D. F. 1989, ApJ, 345

Burns, J. O. 1990, AJ, 99, 14

Dickey, J. M. & Lockman, F. J. 1990, ARA&A, 28, 215

Dopita, M. A., Groves, B. A., Sutherland, R. S., Binette, L., & Cecil, G. 2002, ApJ, 572, 753

Evrard, A. E. 1988, MNRAS, 235, 911

Fukui, Y. & Mizuno, A. 1991, in IAU Symp. 147: Fragmentation of Molecular Clouds and Star Formation A Comparative Study of Star Formation Efficiencies in Nearby Molecular Cloud Complexes., ed. Falgarone, E. and Boulanger, F. and Duvert, G., 275

Gingold, R. A. & Monaghan, J. J. 1977, Mon. Not. R. Astron. Soc., 181, 375

Hernquist, L. & Katz, N. 1989, ApJS, 70, 375

Hu, X. Y. & Adams, N. A. 2006, J. Comp. Phys., 213, 844

Inutsuka, S. 2002, J. Comp. Phys., 213, 238

Katz, A. V. 2001, Physica D, 459

Kompaneets, A. S. 1960, Soviet Physics Doklady, 130, 46

Lada, C. J. & Lada, E. A. 2003, ARA&A, 41, 57

Landau, L. D. & Lifshitz, E. M. 1987, Course of Theoretical Physics, Vol. 6, Fluid Mechanics, 2nd edn. (Oxford: Pergamon Press)

Lucy, L. B. 1977, Astron. J., 82, 1013

Mac Low, M. M. & Ferrara, A. 1999, ApJ, 513, 142

Maciejewski, W. & Cox, D. P. 1999, ApJ, 511, 792

Marri, S. & White, S. D. M. 2003, MNRAS, 345, 561

Mashchenko, S., Couchman, H. M. P., & Wadsley, J. W. 2006, Nature, 442, 539

McCarthy, I. G., Babul, A., Bower, R. G., & Balogh, M. L. 2008, MNRAS, 386, 1309

Monaghan, J. J. 1992, ARA&R, 30, 543

—. 1997, J. Comp. Phys., 136, 298

—. 2005, Rep. Prog. Phys., 68, 1703

Norman, M. L. 2000, Revista Mexicana de Astronomia y Astrofisica Conference Series, 9, 66

Price, D. 2008, J. Comp. Phys.

Price, D. J. & Monaghan, J. J. 2005, MNRAS, 364, 384

Rees, M. J., Begelman, M. C., Blandford, R. D., & Phinney, E. S. 1982, Nature, 295, 17

Ritchie, B. W. & Thomas, P. A. 2001, MNRAS, 374, 743

Rosswog, S. & Price, D. 2007, MNRAS, 379, 833

Ryu, D. & Vishniac, E. T. 1987, ApJ, 313, 820

Sedov, L. I. 1946, Journal of Applied Mathematics and Mechanics, 10, 241

Sod, G. A. 1978, J. Comp. Phys., 27, 1

Spitzer, L. 1978, Physics processes in the interstellar medium (New York, NY: John Wiley & Sons, Inc.)

Springel, V., Di Matteo, T., & Hernquist, L. 2005, MNRAS, 361, 776

Springel, V. & Hernquist, L. 2002, MNRAS, 333, 649

Stil, J. M., Wityk, N. D., Ouyed, R., & Taylor, A. R. 2008, arXiv:0807.0057v1 [astro-ph]

Tasker, E. J., Brunino, R., Mitchell, N. L., Michielsen, D., Hopton, S., Pearce, F. R., Bryan, G. L., & Theuns, T. 2008, arXiv:0808.1844 [astro-ph]

Taylor, G. I. 1950, Proceedings of the Royal Society of London, 201, 159

von Neumann, J. 1941, Shock waves started by an infinitesimally short detonation of given (positive and finite) energy, U.S. Government Document AM-9, National Defense Research Council, Div. 8, Washington, DC, USA

Wada, K. & Norman, C. A. 2001, ApJ, 547, 172

Wadsley, J. W., Stadel, J., & Quinn, T. 2004, New Astronomy, 9, 137

Wesseling, P. 2001, Principles of Computational Fluid Dynamics (Springer-Verlag)

Appendix A

The simulation parameters and analysis tools used for the work done in this thesis can be found at www.imp.mcmaster.ca/~lowmd.